Clays and Clay Minerals, Vol. 62, No. 6, 477–499, 2014.

MINERALOGICAL AND GEOCHEMICAL CHARACTERISTICS AND GENESIS OF THE GÜZELYURT ALUNITE-BEARING KAOLINITE DEPOSIT WITHIN THE LATE MIOCENE GÖRDELES IGNIMBRITE, CENTRAL ANATOLIA, TURKEY

Selahattin Kadir[1,*], Tacit Külah[1], Muhsin Eren[2], Nergis Önalgil[1], and Ali Gürel[3]

[1] Eskişehir Osmangazi University, Department of Geological Engineering, TR-26480 Eskişehir, Turkey
[2] Mersin University, Department of Geological Engineering, TR-33343 Mersin, Turkey
[3] Niğde University, Department of Geological Engineering, TR-51200 Niğde, Turkey

Abstract—The Güzelyurt kaolinite deposit is an important source of raw material for the ceramics industry in Turkey. No detailed mineralogical or geochemical characterizations of this deposit have been undertaken previously and these were the goals of the present study. The Güzelyurt alunite-bearing kaolinite occurs along a fault zone in the Late Miocene Gördeles ignimbrite, which consists of dacitic and andesitic tuffs. Horizontal and vertical mineralogical zonations with gradual transitions were observed within the alteration zone. The inner kaolinite, alunite, and 7 Å halloysite zones progress horizontally outward to a smectite zone; and native sulfur- and cinnabar-bearing alunite with 7 Å halloysite and porous silica zones increase as one progresses up through the profile. Fe-(oxyhydr)oxide phases associated with native sulfur and cinnabar demonstrate that multiple hydrothermal-alteration processes resulted in kaolinization and alunitization of the deposit. The kaolinization of feldspar, Fe-(oxyhydr)oxidation of hornblende and mica, the presence of kaolinite as stacked and, locally, book-like forms, and of 7 Å halloysite tubes, and smectite flakes as a blanket on altered volcanic relicts indicate an authigenic origin for this deposit. The leaching of Si + Mg + K and Ba + Rb, the retention of Sr, the enrichment of light rare earth elements relative to the heavy rare earth elements, and the negative Eu anomalies suggest that fractionation of plagioclase and hornblende occurred within the volcanics. The oxygen- and hydrogen-isotopic values of the kaolinite, 7 Å halloysite, smectite, and smectite + kaolinite fractions reflect a steam-heated environment at temperatures in excess of 100ºC. An increase in the δD and $\delta^{18}O$ values of 7 Å halloysite relative to kaolinite suggests its formation under steam-heated magmatic water, the mixing of steam and meteoric water near the surface, and evaporation. The oxygen- and sulfur-isotopic compositions of alunite suggest the direct influence of steam-derived sulfur. The Güzelyurt alunite-bearing kaolinite deposit is inferred to have formed after an increase in the (Al±Fe)/Si ratio and the leaching of alkali elements, which are driven by the sulfur-bearing low-temperature hydrothermal alteration of feldspar, hornblende, and volcanic glass under acidic conditions within the Neogene dacitic and andesitic tuffs.

Key Words—Alunite with 7 Å halloysite, Geochemistry, Hydrothermal Alteration, Ignimbrite, Kaolinite, Micromorphology, Turkey.

INTRODUCTION

Kaolinite deposits generated by hydrothermal action or weathering, or both, within volcanic units, are common in Anatolia (Kadir and Karakaş, 2002; Arslan *et al*., 2006; Ece and Schroeder, 2007; Ece *et al*., 2008; Kadir and Akbulut, 2009; Kadir *et al*., 2011; Erkoyun and Kadir, 2011; Kadir and Erkoyun, 2013). In the Güzelyurt area, the kaolinite deposit has a reserve of ~2,000,000 tons as estimated by a systematic exploration program of the General Directorate of Mineral Research and Exploration of Turkey (MTA) during the period 1975–1977 (Küçüksille, 1979). A previous study, based on the geology and mineralogy of the Güzelyurt kaolinite deposit and its use as an industrial raw material, was completed by Fujii *et al*. (1995). No detailed information was provided in terms of polarized-light microscopy; differential thermal and thermogravimetric analyses; scanning and transmission electron microscopy; geochemical modeling of mass gains and losses of major, trace, and rare-earth elements during alteration; crystal chemistry; or stable isotope composition of this kaolinite deposit which is an important source of raw materials for the ceramics and paper industries in Turkey. The present study focused on the mineralogy, micromorphology, geochemistry, and stable-isotope geochemistry of the Güzelyurt kaolinites within the volcanic units which developed in a tectonically controlled hydrothermal system. New data are provided to help explain the physicochemical conditions of the hydrothermal alteration processes and genesis of the kaolinite, 7 Å halloysite, and associated alunite within the volcanic units in Anatolia.

* E-mail address of corresponding author:
skadir_esogu@yahoo.com
DOI: 10.1346/CCMN.2014.0620603

GEOLOGICAL SETTING AND GENERAL FEATURES OF THE KAOLINITE DEPOSIT

The basement rocks of the study area consist of Paleozoic metamorphic rocks (calc-schist, quartz-schist,

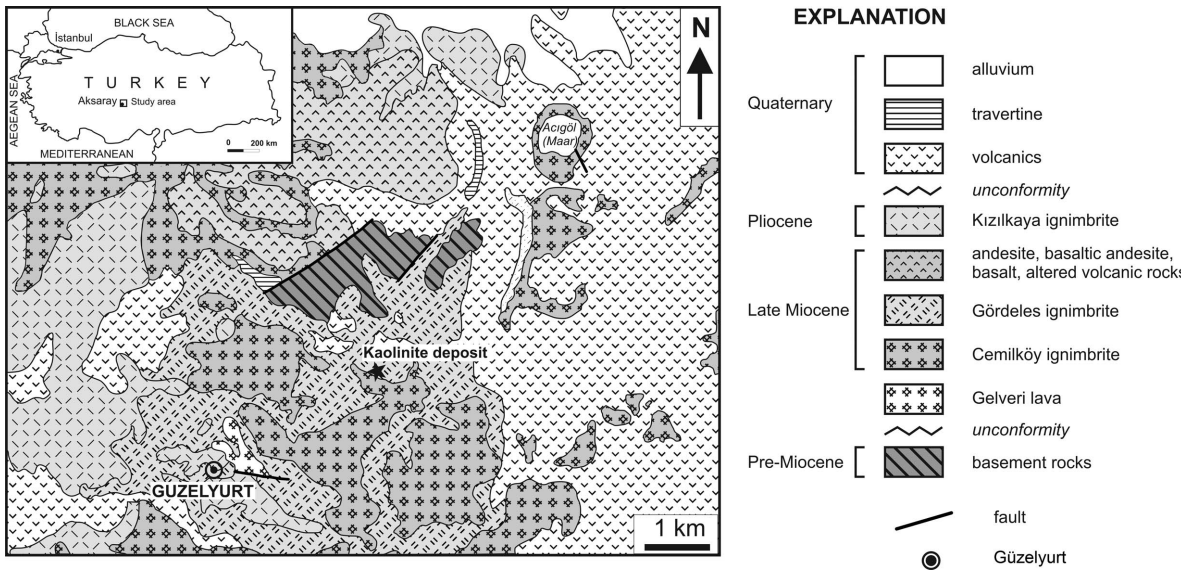

Figure 1. Simplified geological map of the Güzelyurt area (modified from Dönmez *et al.* 2005).

gneiss, and marble) of the Kırşehir Massif. These rocks are overlain tectonically by Mesozoic ophiolitic rocks and were intruded by Senonian plutonic rocks (Figures 1, 2). The basement rocks are overlain unconformably by lacustrine sediments intercalated with volcanic rocks of the Late Miocene Ürgüp Formation. These volcanics are the Sarımadentepe, Cemilköy, and Gördeles ignimbrites, and the Gelveri lava. The Quaternary units consist mainly of volcanics including basalt, andesite, rhyolite, cinder cones, pyroclastics, travertine, and alluvium. The Güzelyurt kaolinite deposit is found within the Ürgüp Formation and extends along a NE–SW-trending normal fault related to the major Tuz Gölü Fault. The kaolinite deposit is ~300 m long, 100 m wide, and 25 m thick (Figures 3, 4), and is underlain mainly by pinkish-white, massive, and fractured marble consisting of coarse- or

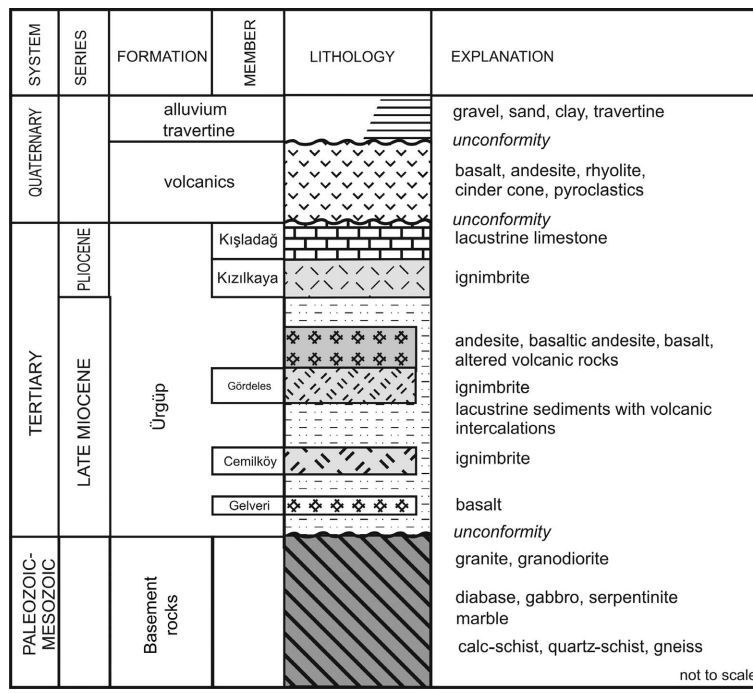

Figure 2. Generalized stratigraphic column of the study area (modified after Dönmez *et al.*, 2005).

https://doi.org/10.1346/CCMN.2014.0620603 Published online by Cambridge University Press

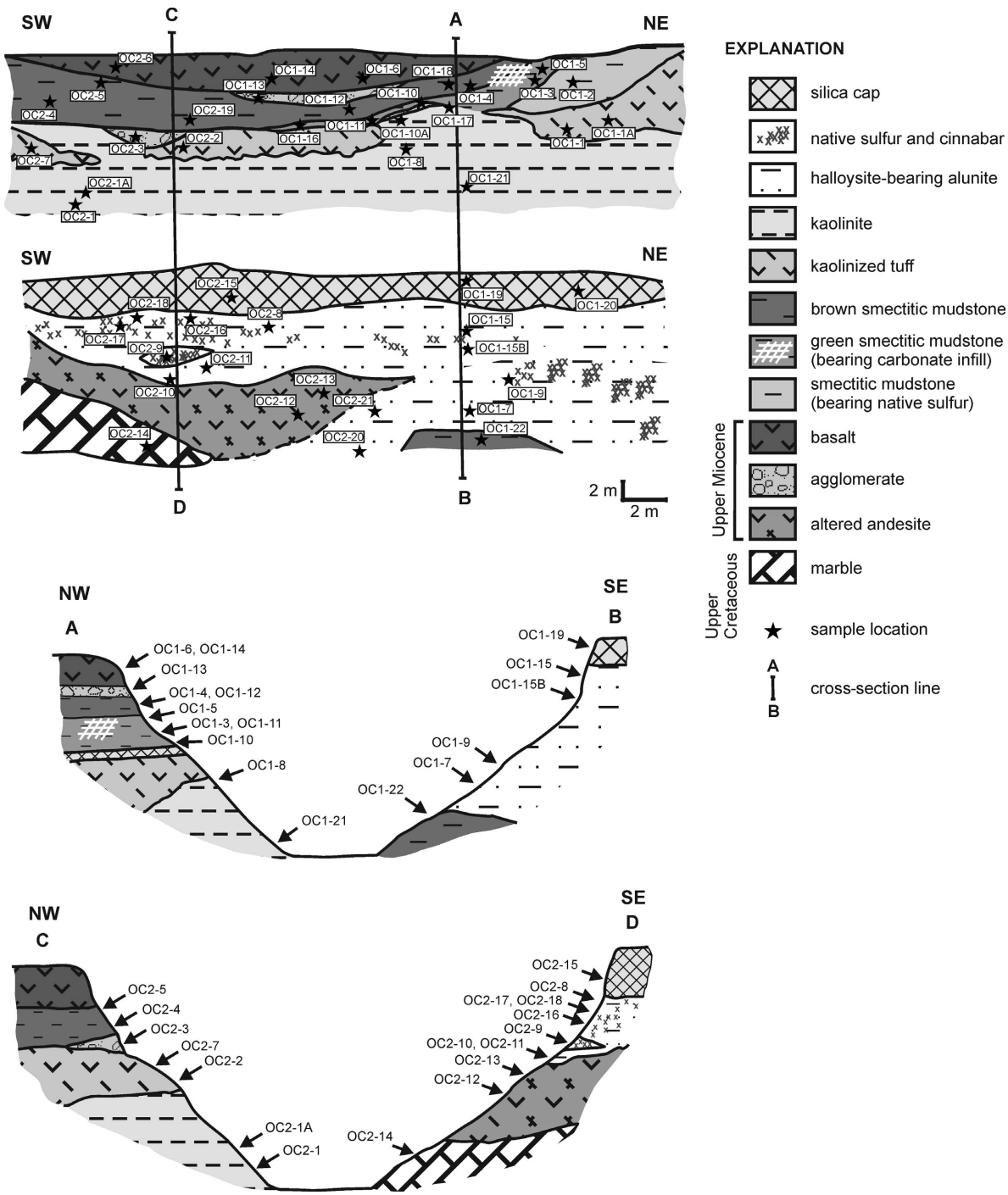

Figure 3. Sketch and profiles of the Güzelyurt kaolinite deposit.

medium-grained calcite crystals. The kaolinite deposit was formed by hydrothermal alteration of dacite- and andesite-type Gördeles ignimbrite (Temel *et al.*, 1995). Alteration zones are present in these deposits. Kaolinized dacitic and andesitic tuffs crop out at the lower part of the deposit, and the alunite + 7 Å halloysite zone crops out in the andesitic unit in the central and upper parts of the deposit. The intensity of kaolinization decreases and alunite increases upward. These units enclose native sulfur and cinnabar disseminations and are covered by a porous silica cap. A smectite zone occurs outside the kaolinite deposit. The lower part of the smectite zone is

https://doi.org/10.1346/CCMN.2014.0620603 Published online by Cambridge University Press

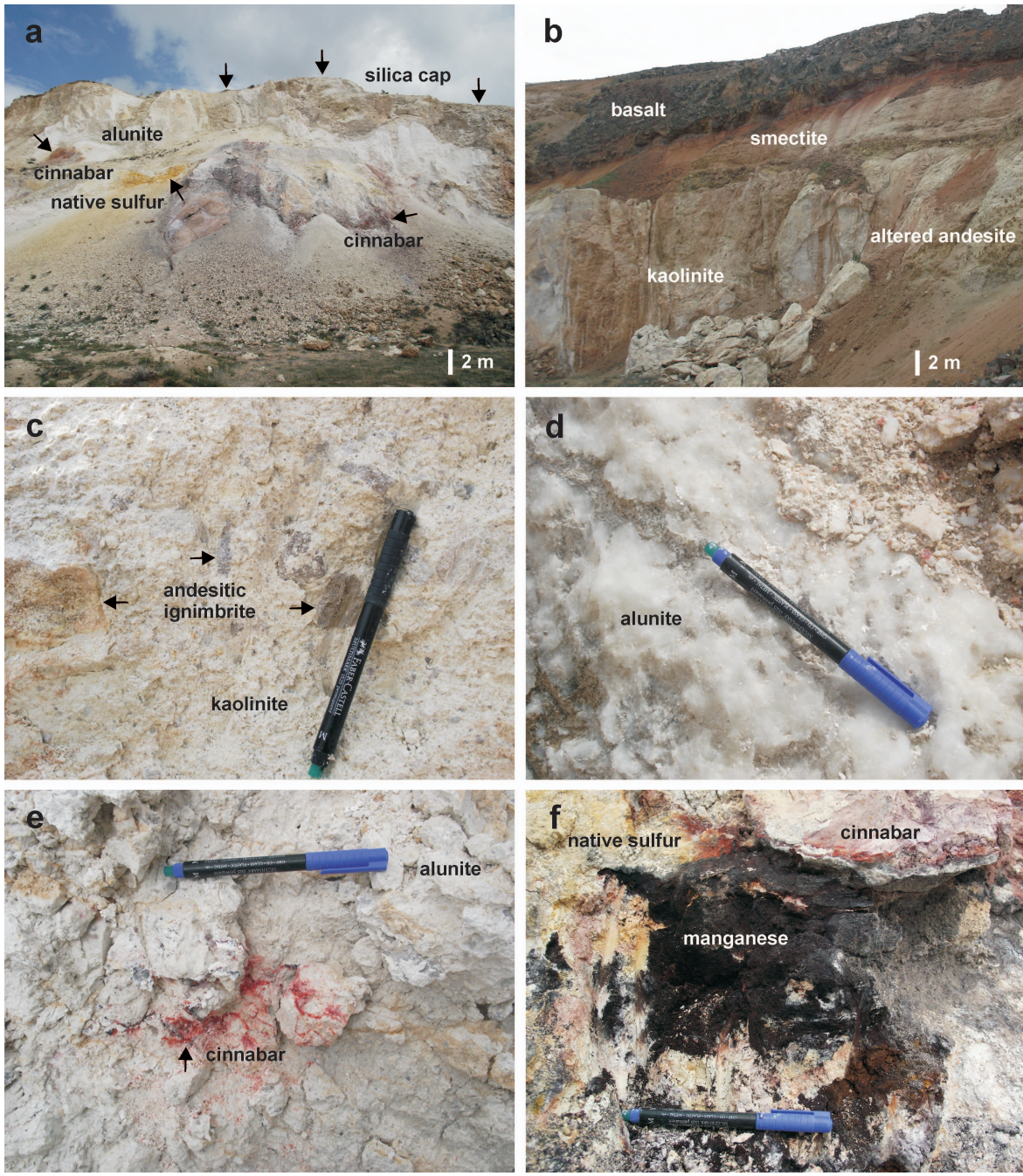

Figure 4. Field view of: (a) silica cap on the uppermost kaolinite deposit; (b) development of smectite between kaolinite and basaltic lava; (c) presence of andesite clasts in kaolinized units; (d) close-up view of alunite; (e) close-up view of the cinnabar associated with alunite; and (f) close-up view of cinnabar, manganese, and native sulfur associated with alunite.

pale green while the upper part is a reddish-brown, laminar, plastic, and silty smectitic mudstone. This mudstone is fractured and encloses light purple-colored native sulfur and cinnabar. The smectite zone also encloses agglomeratic pyroclastic flow lenses that have an andesitic character and are overlain by black, gray–dark gray and brown fractured basaltic lava.

MATERIALS AND METHODS

In the field, typical stratigraphic sections were measured to study vertical and lateral variations within the Güzelyurt kaolinite deposit that occurred in the Gördeles ignimbrite. Characteristic fresh and altered samples were collected (Figure 3) and examined under a polarizing microscope (Nikon-LV 100Pol).

https://doi.org/10.1346/CCMN.2014.0620603 Published online by Cambridge University Press

The mineralogical characteristics of the samples were determined by powder X-ray diffraction (XRD) (Rigaku Geigerflex), scanning electron microscopy (SEM-EDX) (JEOL JSM 84A-EDX), and transmission electron microscopy (TEM) (JEOL JEM-21007). The clay mineralogy was determined after separation of the clay fraction (<2 μm) by sedimentation, followed by centrifugation of the suspension after an overnight dispersion in distilled water. The clay particles were dispersed by ultrasonic vibration for ~15 min. Three oriented specimens of the <2 μm fraction of each sample were prepared by air drying, ethylene-glycol solvation at 60ºC for 2 h, and thermal treatment at 550ºC for 2 h. The mineralogy of the bulk samples was determined by XRD with CuKα radiation and a scanning speed of 1º2θ min^{-1} at the Turkish Petroleum Corporation (TPAO). Semi-quantitative abundances of rock-forming minerals were obtained using Brindley's (1980) external standard method, whereas the relative abundances of clay-mineral fractions were determined using their basal reflections and the mineral intensity factors described by Moore and Reynolds (1989).

Representative clay-dominated bulk samples were prepared for the SEM-EDX analysis by adhering the fresh, broken surface of each sample onto an aluminum sample holder with double-sided tape and coating thinly (350 Å) with gold using a Giko ion coater. The clay particles for TEM analysis were dispersed in an ultrasonic ethanol bath for ~30 min, and one drop of each clay suspension was placed on carbon-coated copper grids and dried at room temperature.

Differential thermal and thermogravimetry analyses (DTA-TG Rigaku TAS 100 E) were performed on the selected samples at Eskişehir Osmangazi University. The DTA-TG curves were obtained from 10 mg of powdered sample in a Pt sample holder, heated at an average rate of 10ºC/min with an alumina reference.

Chemical analyses of 20 fresh and altered volcanic whole-rock samples were performed at the Acme Analytical Laboratories Ltd. (Canada) using inductively coupled plasma–atomic emission spectroscopy (ICP-AES) for major and trace elements and inductively coupled plasma–mass spectroscopy (ICP-MS) for rare-earth elements (*REE*). The detection limits for the analyses were between 0.01 and 0.1 wt.% for major elements, between 0.1 and 5 ppm for trace elements, and between 0.01 and 0.5 ppm for the *REE*.

Enrichment and depletion of elements were estimated using the procedure of MacLean and Kranidiotis (1987). In these calculations, zirconium was assumed to be the most immobile element, based on calculated correlation coefficients with other elements. All samples were grouped on the basis of degree of alteration (average result from each group), and the gains and losses of components were calculated using a starting mass of 100 g of average fresh, anhydrous sample. The equation used in calculations can be written for SiO_2 (MacLean and Kranidiotis, 1987) as follows:

$$SiO_2 = \frac{SiO_2 \text{ wt.\% altered}}{\text{Zr ppm altered}} \times \text{Zr ppm fresh}$$

Gain and loss of mass (ΔC_i) for each element were determined by subtracting the calculated values of reconstructed compositions (RC) from the concentrations of components in the least-altered samples using the formula given above.

Approximate structural formulae for kaolinite, 7 Å halloysite, and smectite were determined for the <2 μm clay samples with the largest 7 Å halloysite and smectite contents. These samples were sieved to <2 mm; 100 g of the sieved sample was mixed with deionized water and disaggregated using a Stir-pak mixer head and mixer controller. The <2 μm fractions were subsequently isolated from the silt (2–50 μm) using repeated siphoning of the dispersed material. The clay fractions were separated by sedimentation of the suspension after 24 h of dispersion in distilled water and removal of the upper 5 cm, followed by centrifugation for 10 min at $2451 \times g$ (4000 rpm) using a Hettich Rotofix 32A centrifuge. The silica and phosphorous content were corrected for impurities such as amorphous materials and accessory P_2O_5, which was not removed and not detected by XRD.

The approximate structural formulae of kaolinite and 7 Å halloysite were calculated based on $O_{10}(OH)_8$, and of smectite based on $O_{20}(OH)_4$ by the following procedure: the tetrahedral sites of kaolinite and of 7 Å halloysite were filled with Si and Al to a sum of four, and tetrahedral sites of smectite were filled with Si and Al as needed to a sum of eight. The remaining Al in kaolinite, 7 Å halloysite, and smectite was assigned to octahedral sites. All iron, considered to be ferric, and all Mn and Ti were assigned to the octahedral site. Ca, Na, and K were deemed to be exchangeable interlayer cations.

Eight kaolinite-, 7 Å halloysite-, smectite-bearing clay fractions were purified and analyzed for the H and O stable isotopes in the Cornell Isotope Laboratory at Cornell University, New York. The isotope corrections were performed using a two-point normalization (regression) based on international standards (IAEA CO-1 and IAEA CO-8) for $\delta^{18}O$ and CH-7 and benzoic acid for δD. The analyses were performed using a Thermo Delta V isotope ratio mass spectrometer interfaced with a temperature-conversion elemental analyzer. The delta values for ^2H and ^{18}O were measured against the primary reference scale of Clayton and Mayeda (1963). The data are reported in standard delta notation as per mil deviations from V-SMOW (Vienna Standard Mean Ocean Water). The standard deviation for internal standard benzoic acid for $\delta^{18}O$ is 1.01‰ and for δD is 1.24‰.

The $\delta^{34}S + \delta^{18}O$ were determined on seven alunite samples which were selected carefully by handpicking under a binocular microscope. Stable-isotope analyses ($\delta^{34}S + \delta^{18}O$) were conducted at the University of Arizona Department of Geosciences using an MAT

https://doi.org/10.1346/CCMN.2014.0620603 Published online by Cambridge University Press

261-8 mass spectrometer. The results of $\delta^{34}S$ (referenced to V-CDT – Vienna Canyon Diablo Troilite) and $\delta^{18}O_{sulfate}$ (referenced to V-SMOW) are listed in Table 6.

$\delta^{34}S$ was measured on SO_2 gas in a continuous-flow gas-ratio mass spectrometer (ThermoQuest Finnigan Delta PlusXL, Tucson, Arizona, USA). The samples were combusted at 1030ºC with O_2 and V_2O_5 using an elemental analyzer (Costech, Tucson, Arizona, USA) coupled to the mass spectrometer. Standardization is based on international standards OGS-1 and NBS123 (Hosono *et al*. 2014), and several other sulfide and sulfate materials for sulfur that have been compared between laboratories. Calibration is linear in the range −10 to +30‰. Precision is estimated to be ±0.15‰ or better (1σ) based on repeated internal standards.

The $\delta^{18}O$ of sulfate was measured on CO gas in a continuous-flow gas-ratio mass spectrometer (Thermo Electron Delta V, Tucson, Arizona, USA). The samples were combusted with excess C at 1350ºC using a thermal combustion elemental analyzer (ThermoQuest Finnigan, Tucson, Arizona, USA) coupled to the mass spectrometer. Standardization is based on international standard OGS-1. Precision is estimated to be ±0.4‰ or better (1σ), based on repeated internal standards.

RESULTS

Mineralogical determinations

The dacitic and andesitic ignimbrite has a porphyritic texture and consists of plagioclase, hornblende, biotite, andesitic rock fragments, and devitrified volcanic glass (Figure 5). The plagioclase often shows argillization, whereas the hornblende and mica crystals are (oxyhydr)-oxidized (Figure 5a–d).

The XRD analyses of the bulk samples and clay fractions taken from the Güzelyurt kaolinite deposit are listed in Table 1 and traces are shown in Figure 6. Kaolinite, 7 Å halloysite, alunite, and smectite-type alteration products are accompanied by feldspar, quartz, and opal-CT and locally by calcite and accessory hornblende and dolomite. Kaolinite and alunite are present in

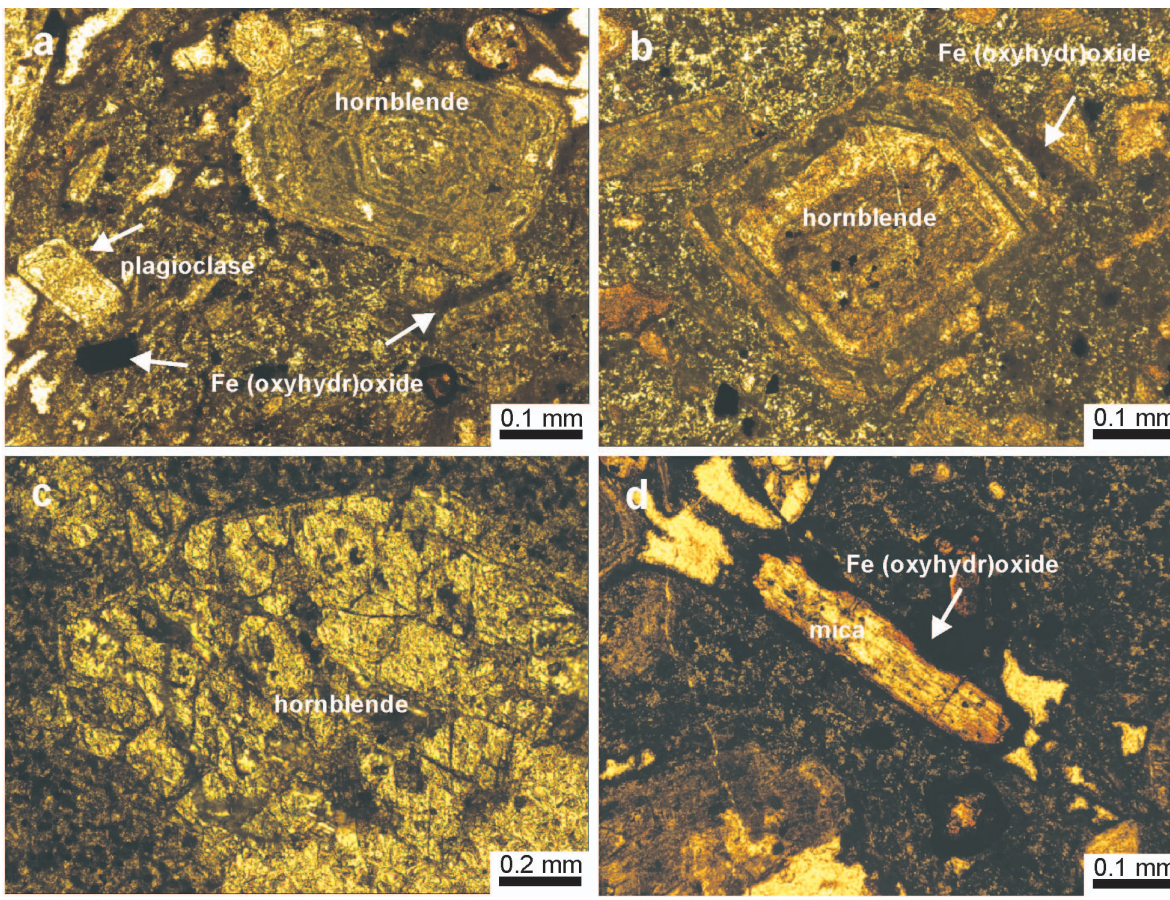

Figure 5. Photomicrographs of: (a,b) Fe-(oxyhydr)oxide hornblende crystals; plain-polarized light (OC2-3); (c) altered amphibole crystal associated with Fe-(oxyhydr)oxide; plain-polarized light (OC1-4); and (d) Fe-(oxyhydr)oxide mica crystal; plain-polarized light (OC2-3).

https://doi.org/10.1346/CCMN.2014.0620603 Published online by Cambridge University Press

Table 1. Mineralogical compositions of the fresh and altered samples.

Sample	Rock type	kln	hal	alu	sme	qz	opl	hbl	fsp	dol
OC1-1	Altered tuff		+	+++		acc				
OC1-1A	Altered tuff			+++++						
OC1-2	Mudstone	++++			+					
OC1-3	Mudstone	+			++++	acc			acc	
OC1-4	Mudstone			acc	+++++			acc		
OC1-5	Mudstone				+++++					
OC1-7	Altered tuff	+		++++		acc				
OC1-8	Altered tuff	+++			++	acc				
OC1-10	Altered tuff	acc			++++	acc			acc	
OC1-10A	Altered tuff	++++			+	acc				
OC1-15	Altered tuff		++++			+	acc			
OC1-15B	Altered tuff		++++	++		acc	acc			
OC1-16	Mudstone	+			+++++	acc			acc	
OC1-17	Mudstone	++++			+	acc				
OC1-18	Mudstone				+++++					
OC1-19	Silica					+++	++			
OC1-20	Silica					+++++				
OC2-1	Altered tuff	++++		+		acc	acc			
OC2-2	Altered tuff		++++	+		acc	acc			
OC2-5	Mudstone				+++++	acc			acc	
OC2-7	Altered tuff		++++	+		acc	acc		acc	
OC2-8	Altered tuff			+++++					acc	acc
OC2-9	Mudstone	acc		+++++		acc				
OC2-10	Altered tuff			+++++		acc	acc		acc	
OC2-11	Altered tuff	acc		+++++			+			
OC2-12	Altered tuff			+++		+	acc			
OC2-13	Altered tuff			+		+	+++	acc		
OC2-15	Silica					+++++				
OC2-16	Altered tuff		++++	+		acc				
OC2-17	Altered tuff		++++	+	+	acc				
OC2-18	Altered tuff		++	++++			acc			
OC2-19	Mudstone	acc			+++++	acc			acc	
OC2-20	Altered tuff			+++++		acc				
OC2-21	Altered tuff			+++++		acc	+			

kln: kaolinite, hal: 7 Å halloysite, alu: alunite, sme: smectite, qz: quartz, opl: opal-CT, hbl: hornblende, fsp: feldspar, dol: dolomite, acc: accessory, +: relative abundance of mineral.

the central part of the deposit. Kaolinite appears in the NW part of the deposit, whereas alunite and alunite-bearing kaolinite are present in the SE part of the deposit. Kaolinite dominates in the lower level, and 7 Å halloysite-bearing alunite dominates in the middle and upper levels of the SE part of the kaolinite deposit. An inverse relationship exists between kaolinite and alunite + 7 Å halloysite in the deposit. Smectite was formed as a result of the alteration of basaltic units and predominates in the green and reddish-brown mudstones, stratigraphically above and laterally away from the deposit.

Kaolinite and 7 Å halloysite are identified by sharp peaks at ~7.18 and 3.58 Å and non-basal reflections of doublets and triplets at 4.47, 4.37, 2.57, 2.50, 2.38, 2.34, and 2.30 Å (Brindley, 1980; Wilson, 1987) (Figure 6). The basal reflection at 7.2 Å is not affected by ethylene-glycol treatment. The 7.2 Å peak collapsed at 550ºC due to dehydroxylation. Alunite is identified by sharp peaks at 5.72, 4.95, 3.49, 2.98, 2.88, 2.28, 1.90, and 1.49 Å.

Smectite was identified by a narrow peak at 15.17 Å which expanded to 18.09 Å with ethylene-glycol treatment and then collapsed to 10.39 Å after heating at 550ºC for 2 h (Figure 6). The d_{060} value of 1.50 Å indicated dioctahedral smectite (Moore and Reynolds, 1989). The XRD background of some of the alunite-kaolinite-bearing samples is slightly elevated, possibly due to the presence of a poorly crystalline phase. The opal-CT is recognized by 4.32 and 4.06 Å reflections and a slight elevation of the XRD background of some of the kaolinite-bearing samples, possibly due to the presence of a poorly crystalline phase.

SEM-EDX, TEM, and mineral chemistry

Kaolinite occurs as platy crystals with euhedral to subhedral hexagonal outlines, mostly arranged face-to-face in elongated book-like stacks or as vermiform crystals (Figure 7a,b). The kaolinite plates have dimensions of 2 μm × 5 μm. In the altered volcanic units, 7 Å

https://doi.org/10.1346/CCMN.2014.0620603 Published online by Cambridge University Press

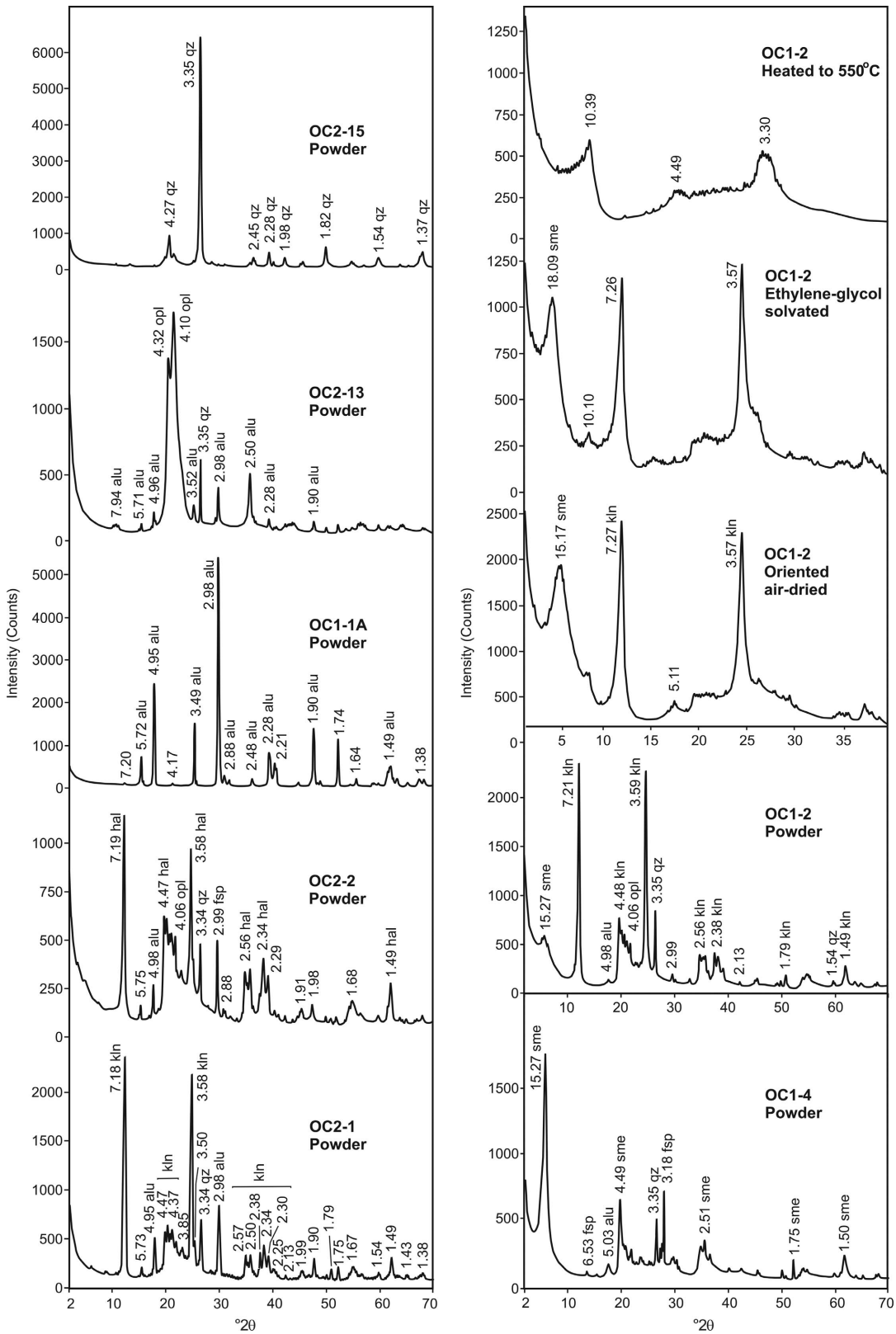

Figure 6. XRD patterns of altered volcanic samples. kln: kaolinite, hal: 7 Å halloysite, alu: alunite, sme: smectite, qz: quartz, fsp: feldspar, opl: opal-CT.

https://doi.org/10.1346/CCMN.2014.0620603 Published online by Cambridge University Press

halloysite occurs as masses of rod-like forms coexisting with cubic alunite crystals (2–7 μm) and devitrified volcanic glass (Figure 7c–f).

Smectite crystals exhibit a well defined, web-like morphology, which developed authigenically as grain coatings on relict feldspar and volcanic grains (Figure 7g–j). These individual flaky crystals range from 1 to 5 μm in diameter.

The silica-cap samples are characterized by lepispheres composed of sub-rounded accumulations of acicular crystals (~3 μm) of opal-CT (Figure 7k). The gypsum crystals have a highly porous, elongate, irregular prismatic lath texture (Figure 7l).

The approximate structural formulae of kaolinite, 7 Å halloysite, and smectite were calculated from chemical analyses of the clay fractions (Table 2). The resulting

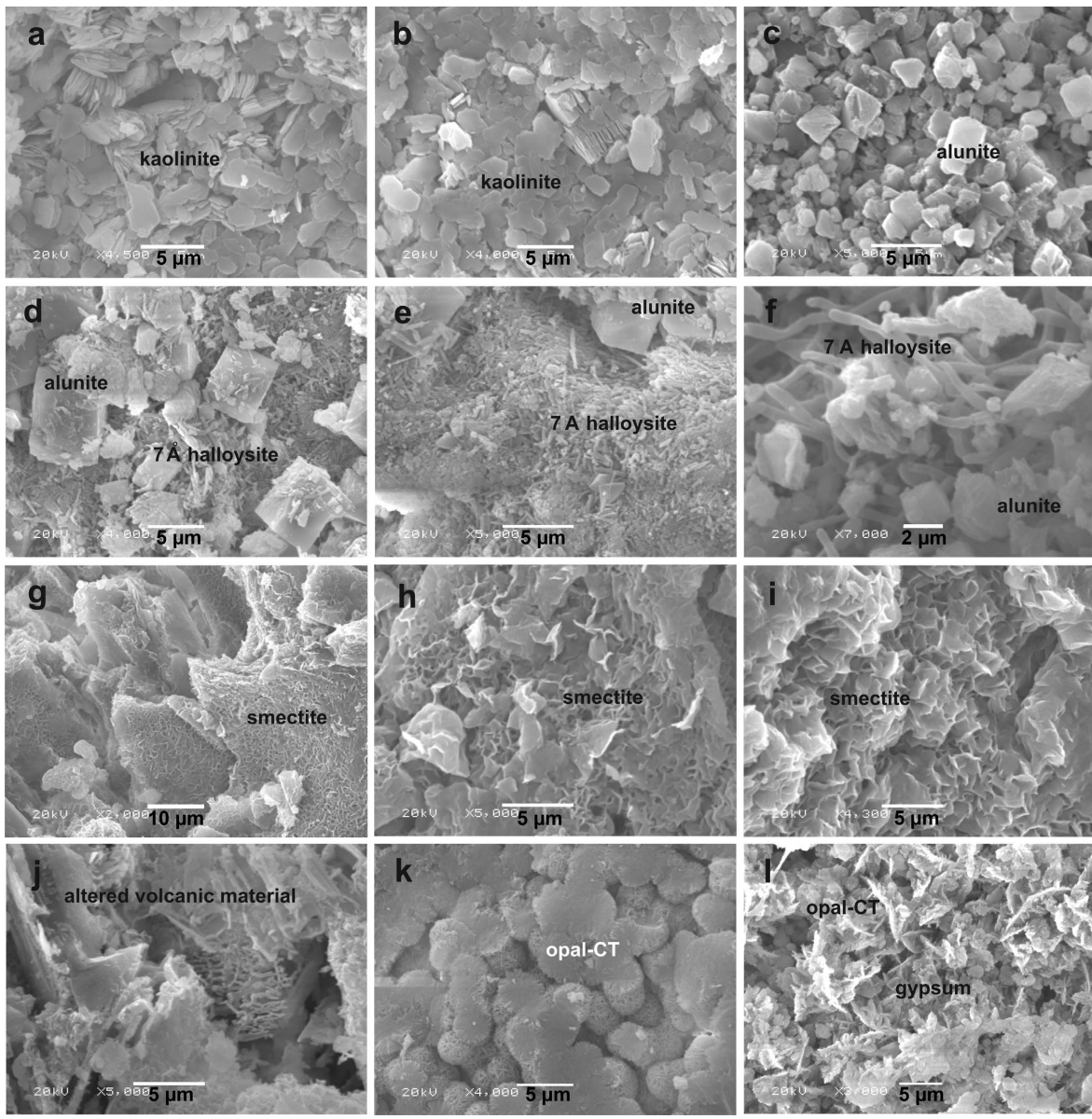

Figure 7. SEM images of: (a,b) euhedral kaolinite-crystal stacks, with vermiform structure (OC2-1); (c) euhedral cubic alunite crystals (OC1-1A); (d) euhedral cubic alunite crystals in association with rod-like 7 Å halloysite (OC2-2); (e) subparallel 7 Å halloysite rod coexisting with alunite in a microfracture (OC2-2); (f) development of a sub-parallel 7 Å halloysite rod between alunite crystals (OC1-1); (g–i) the formation of smectite flakes in dissolution voids of altered volcanic materials (OC1-4); (j) highly altered volcanic materials associated with a highly porous structure (OC1-2); (k) acicular crystal accumulation and development of lepisphere structures of opal-CT coexisting with minor gypsum crystals (OC2-15); and (l) prismatic laths of gypsum with a rosette-like structure (OC2-15).

https://doi.org/10.1346/CCMN.2014.0620603 Published online by Cambridge University Press

Table 2. Chemical compositions (wt.%) and structural formulae for purified kaolinite, 7 Å halloysite, and smectite samples.

Major oxides (wt.%)	OC2-1 kaolinite	OC2-2 7 Å halloysite	OC2-5 smectite
SiO_2	44.14	44.16	51.79
Al_2O_3	36.40	36.09	15.61
ΣFe_2O_3	1.71	2.28	7.86
MgO	0.39	0.71	3.14
CaO	0.34	0.61	2.21
Na_2O	0.62	0.05	0.20
K_2O	1.27	0.34	0.47
TiO_2	0.96	0.65	0.43
MnO	0.01	0.01	0.06
LOI	14.00	14.90	17.90
Total	99.84	99.80	99.67
CIA	94.23	97.30	84.42
SiO_2/Al_2O_3	1.21	1.22	3.31
SiO_2/R_2O_3	1.16	1.15	2.20
Tetrahedral			
Si	3.90	3.92	7.67
Al	0.10	0.08	0.33
Σ	4.00	4.00	8.00
Octahedral			
Al	3.69	3.69	2.39
Fe	0.11	0.15	0.88
Mg	0.05	0.09	0.69
Ti	0.06	0.04	0.05
Mn	0.001	0.001	0.01
Σ	3.91	3.98	4.02
Interlayer			
Ca	0.03	0.06	0.35
Na	0.11	0.01	0.06
K	0.14	0.04	0.09
Σ	0.28	0.11	0.51
Tetrahedral charge	0.10	0.09	0.32
Octahedral charge	0.24	0.08	0.60
Total charge	0.34	0.17	0.92
Interlayer charge	0.31	0.16	0.85
xt/xo	0.41	1.02	0.53

formulae of kaolinite, 7 Å halloysite, and smectite are as follows: $(Si_{3.90}Al_{0.10})(Al_{3.69}Fe_{0.11}Mg_{0.05}Ti_{0.06}Mn_{0.001})(Ca_{0.03}Na_{0.11}K_{0.14})O_{10}(OH)_8$, $(Si_{3.92}Al_{0.08})(Al_{3.69}Fe_{0.15}Mg_{0.09}Ti_{0.04}Mn_{0.001})(Ca_{0.06}Na_{0.01}K_{0.04})O_{10}(OH)_8$, and $(Si_{7.67}Al_{0.33})(Al_{2.39}Fe_{0.88}Mg_{0.69}Ti_{0.05}Mn_{0.01})(Ca_{0.35}Na_{0.06}K_{0.09})O_{20}(OH)_4$, respectively.

The tetrahedral sites of kaolinite, 7 Å halloysite, and smectite are filled with Si cations which have been substituted by some of the Al. Al^{3+} is the abundant octahedral cation of kaolinite, 7 Å halloysite, and smectite. Traces of Fe^{3+}, Mg, Ti, and Mn, referred to as 'R', substitute for some of the Al. Thus, these clays are characterized as Fe-bearing kaolinite, 7 Å halloysite, and smectite.

The SiO_2/Al_2O_3 and SiO_2/R_2O_3 ratios of 1.21 and 1.16 for pure kaolinite, of 1.22 and 1.15 for pure 7 Å halloysite, and of 3.31 and 2.20 for pure smectite, respectively, are consistent with the ideal ratios reported by Jepson and Rowse (1975).

Determinations by TEM revealed that the Güzelyurt kaolinite exhibits euhedral, hexagonal forms with regular outlines characteristic of well crystallized kaolinite (Figure 8a–f). The kaolinite plates are up to 200 nm × 300 nm in size and 10–20 nm thick. The 7 Å halloysite exhibits tube-like forms, with a 70–100 nm diameter, and are ~10 nm thick and 450 nm long (Figure 8d–f).

DTA-TG

The DTA-TG curves for kaolinite, 7 Å halloysite, alunite, and smectite represent typical thermal reactions and are consistent with the results of XRD, SEM-EDX, TEM, and chemical analyses. The reaction of the Güzelyurt kaolinite and 7 Å halloysite upon heating

https://doi.org/10.1346/CCMN.2014.0620603 Published online by Cambridge University Press

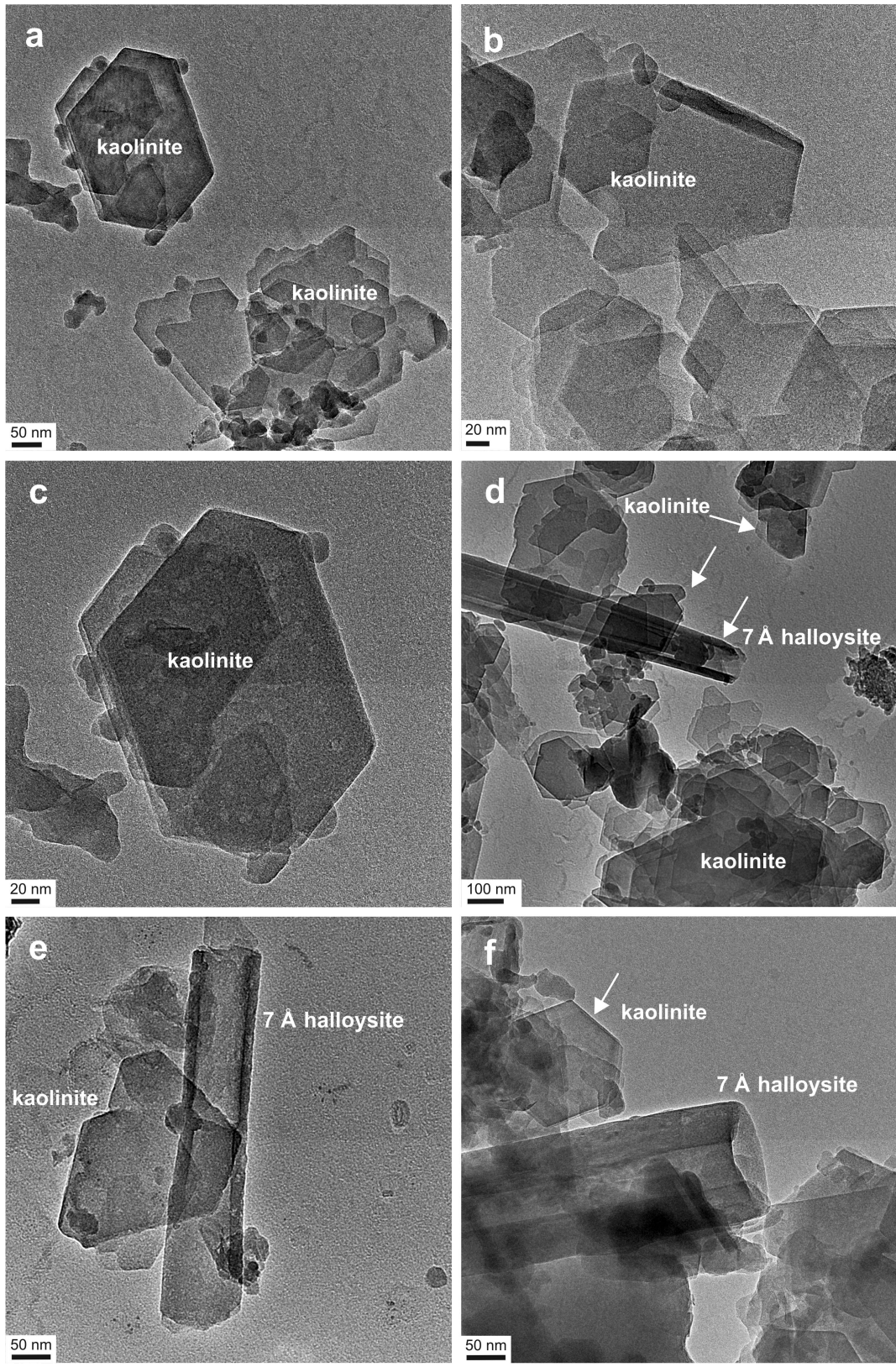

Figure 8. TEM image of: (a–c) hexagonal platy kaolinite crystals (OC2-1) and (d–f) rod-like 7 Å halloysite (OC2-2).

https://doi.org/10.1346/CCMN.2014.0620603 Published online by Cambridge University Press

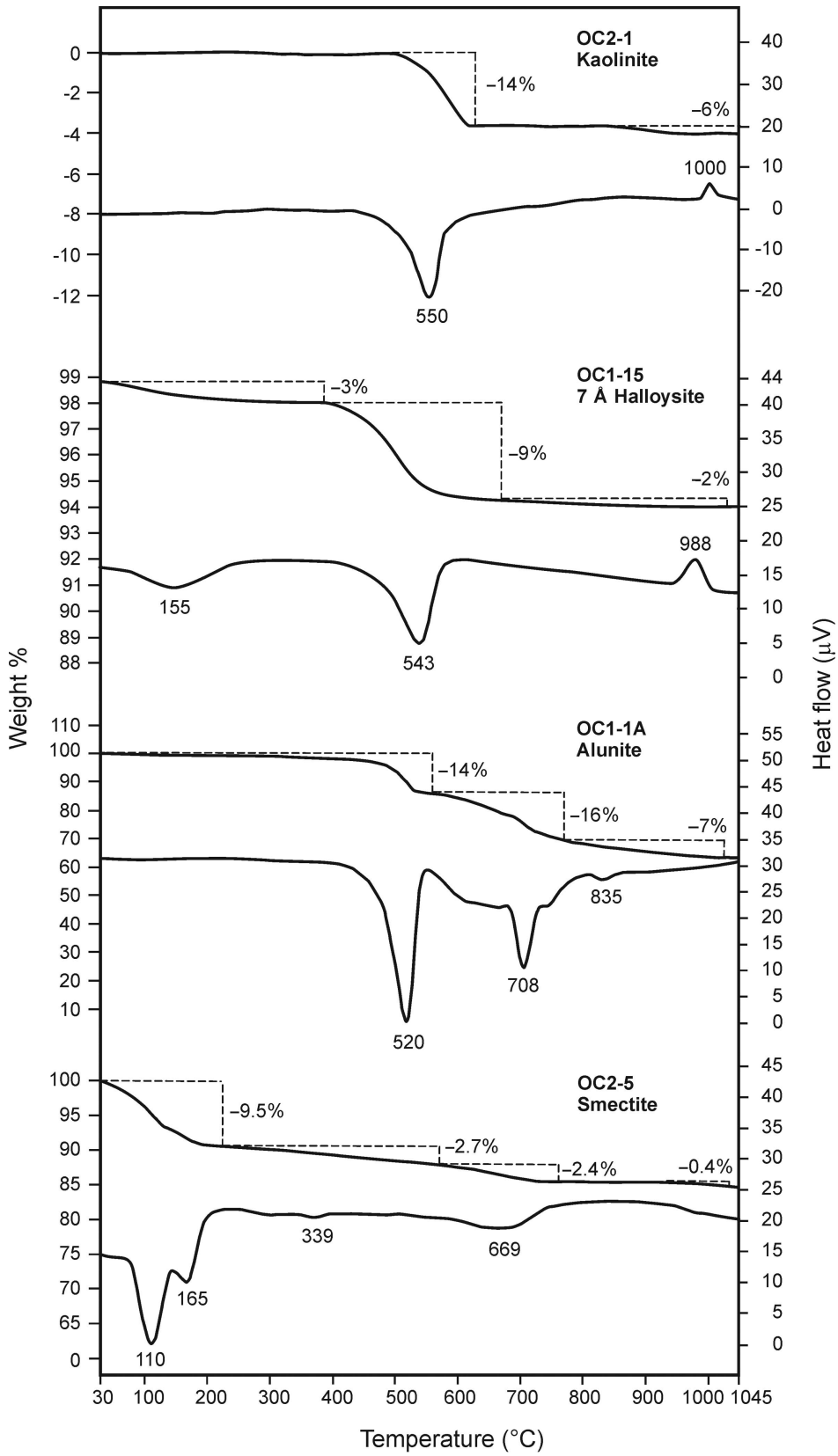

Figure 9. DTA-TG curves for kaolinite (OC2-1), 7 Å halloysite (OC1-15), alunite (OC1-1A), and smectite (OC2-5) samples.

https://doi.org/10.1346/CCMN.2014.0620603 Published online by Cambridge University Press

show similar peaks (Figure 9). Kaolinite sample OC2-1 shows a strong and symmetrical endothermic peak at ~550ºC (weight loss = 14%) and an exothermic peak at 1000ºC (weight loss = 6%). The endothermic and exothermic peaks are attributed to the dehydroxylation of kaolinite rather than dickite and nacrite. Both dickite and nacrite have dehydroxylation peaks at higher temperatures, ~680ºC (MacKenzie, 1957; Paterson and Swaffield, 1987; Yuan and Murray, 1993; Chen *et al*., 2001; Lanson *et al*., 2002; Njoya *et al*., 2006). The 7 Å halloysite sample OC1-15 is characterized by two endothermic peaks at 155ºC (weight loss = 3%) and 543ºC (weight loss = 9%) and an exothermic peak at 988ºC (weight loss = 2%) (MacKenzie, 1957; Paterson and Swaffield, 1987).

The DTA-TG curves of alunite sample OC1-1A exhibited the first strong asymmetric endothermic peak at a temperature of 520ºC (weight loss = 14%), the second widespread peak at 708ºC (weight loss = 16%), and the last and faintest peak at 835ºC (mean 835ºC, weight loss = 7%) (Figure 9). The first endothermic peak is attributed to the initial dehydroxylation, the second and the final peaks represent elimination of sulfur due to the decomposition of alunite structure, as reported by Ece and Schroeder (2007).

The DTA-TG analysis of the smectite-dominated OC2-5 sample shows a large asymmetric endothermic peak at ~110–165ºC (weight loss 9.5%), a medium-sized endothermic peak at ~339ºC (weight loss = 2.7%), and a final, small endothermic peak at 669ºC (weight loss = 2.4%) (Figure 9). Similar peaks were obtained by Mackenzie (1957), Imai *et al*. (1969), Smykatz-Kloss (1974), Paterson and Swaffield (1987), and Jones and Galán (1988). The DTA curve shows a decline starting at ~900ºC, possibly reflecting decomposition to sintering phases.

Geochemistry

Chemical analyses of the Güzelyurt kaolinite samples are given in Table 3. The samples are characterized by large values of Al_2O_3 (avg. 11.14–23.87%), Fe_2O_3 (avg. 2.7–4.71%), SiO_2 (avg. 55.1–39.3%), and loss on ignition (LOI) (avg. 17.4–25.07%). The LOI is an important indicator for degree of alteration. Compared with kaolinite, the amount of Al_2O_3 + K_2O + LOI and SO_3 + Hg increases upward through the deposit sequence, concomitant with an increase in alunite and 7 Å halloysite. Sample OC1-9 is dominated by SO_3 (42.66%) and Hg (9.55 ppm), however, reflecting the presence of native sulfur and cinnabar, respectively.

Using mass gains and losses (MacLean and Kranidiotis, 1987), enrichments and depletions of major and trace elements from fresh to altered samples were observed (Table 4; Figure 10). Si, Mg, K, Ba, Rb, Y, and Pb were depleted during the alteration of feldspar, hornblende, biotite, and volcanic glass derived from the volcanic units. Conversely, Al, Fe, Ca, Hg, Sr, V, As, and Σ*REE* were enriched during this process.

Light *REE*s (*LREE*) such as La, Ce, and Nd were enriched relative to the heavy *REE*s (*HREE*) (Figure 11). The *LREE*s had an increasing intensity of degree of alteration within the volcanic units and exhibited a negative Eu anomaly in the kaolinized and alunitized materials.

Stable-isotope geochemistry

The results of D- and O-isotopic analyses of purified kaolinite, 7 Å halloysite, smectite, and smectite + kaolinite fractions are listed in Table 5 and plotted in Figure 12. The δD and $\delta^{18}O$ values of kaolinite and 7 Å halloysite range from −132.92‰ to −101.81‰, and from 0.56‰ to 7.64‰, respectively. The δD and $\delta^{18}O$ values of the smectite and smectite + kaolinite fraction

Table 3. Chemical compositions of the fresh and altered tuff samples.

Major oxides	Fresh tuff				Altered tuff						
(wt.%)	OC3-3	OC3-6	OC3-7	Average	OC1-1	OC1-1A	OC1-2	OC1-4	OC1-7	OC1-8	OC1-9
SiO_2	70.2	57.3	37.9	55.1	37.2	2.3	56.6	52.5	40.6	59.6	<0.1
Al_2O_3	9.25	14.06	10.1	11.14	31.10	36.47	23.81	16.52	22.45	22.78	<0.01
ΣFe_2O_3	3.49	2.08	2.53	2.7	0.38	0.34	3.16	5.8	0.08	1.59	<0.01
MgO	0.8	0.58	22.21	7.86	0.22	0.19	0.6	2.24	0.2	0.75	32.91
CaO	0.15	0.1	1.18	0.48	0.15	0.02	0.97	2.64	0.03	0.72	<0.01
Na_2O	0.76	0.54	1.4	0.9	0.94	3.50	0.03	0.63	0.96	0.1	<0.01
K_2O	3.03	4.24	1.55	2.94	2.60	5.13	0.33	0.97	4.41	0.49	<0.01
MnO	0.04	0.02	0.43	0.16	<0.01	<0.01	0.02	0.04	<0.01	0.01	<0.01
TiO_2	0.56	0.4	0.29	0.42	0.29	0.01	0.7	0.67	0.52	0.44	<0.01
P_2O_5	0.25	0.43	0.07	0.25	0.27	0.45	0.08	0.07	0.27	0.08	<0.01
Cr_2O_3	0.014	0.011	0.009	0.011	0.002	0.006	0.005	0.009	0.005	0.002	0.003
LOI	11.45	19.75	20.99	17.4	26.57	43.04	14.56	18.11	29.64	14.04	21.02
Total	100.17	99.76	98.81	99.58	99.84	91.63	100.88	100.23	99.26	100.63	53.96
TOT/C	0.32	0.13	4.31	1.59	0.05	0.07	0.02	0.03	0.02	0.02	<0.02
TOT/S	1.81	4.97	<0.02	2.26	5.48	14.15	0.13	0.03	8.05	0.08	18.03
SO_3	0.112	0.454	1.762	0.776	0.157	6.750	0.003	0.41	0.679	0.028	42.662
V_2O_5	0.018	0.012	0.01	0.013	0.020	0.034	0.022	0.017	0.028	0.016	<0.002

https://doi.org/10.1346/CCMN.2014.0620603 Published online by Cambridge University Press

Trace elements (ppm)											
Cu	<0.001	<0.001	<0.001	0.001	<0.001	<0.001	<0.001	<0.001	<0.001	<0.001	<0.001
Ni	0.003	0.001	0.003	0.002	<0.001	0.002	0.008	<0.001	<0.001	<0.001	<0.001
Pb	0.012	<0.001	<0.001	0.004	<0.001	0.006	<0.001	<0.001	<0.001	<0.001	<0.001
Sr	0.084	0.095	0.02	0.066	0.131	0.205	0.027	0.017	0.085	0.024	0.018
Zn	0.003	0.002	0.006	0.004	0.002	0.002	0.006	0.009	0.002	0.005	0.002
Ba	1563	2666	1184	1804	956	1726	157	216	576	273	<1
Be	<1	<1	<1	1	<1	<1	<1	2	<1	2	<1
Co	1.7	0.2	16.5	6.1	0.2	<0.2	1.5	12.1	<0.2	1.2	<0.2
Cs	14.7	28.3	26.4	23.1	15.9	1.9	29.7	17.9	21.4	49.4	<0.1
Ga	39.9	49.4	11.3	33.5	15.9	25.9	21.3	17.5	45.6	17.4	<0.5
Hf	7.2	4.9	3.9	5.3	1.5	<0.1	7	5.2	8.4	5.7	<0.1
Nb	15.8	11.3	8.7	11.9	4.3	0.2	17.9	12.2	26.1	13.6	<0.1
Rb	78.3	75	90.2	81.2	33.9	82.1	19	77.1	48.6	51.3	<0.1
Sn	1	<1	<1	1	<1	<1	3	1	2	1	<1
Sr	861.3	1005.3	216	694.2	1381	2236	277.9	156.5	884.8	195.3	228.5
Ta	1.1	0.9	0.5	0.8	0.2	<1	1.1	0.7	1.5	1.1	<0.1
Th	57.5	32.8	12.9	34.4	24.0	34.1	17.4	15.8	20.5	20.1	0.8
U	4.6	2.9	2.3	3.3	1.9	0.6	1.5	1.4	5	3.3	<0.1
V	95	71	57	74	114	208	115	97	162	93	<8
W	2.2	1.4	1.7	1.8	1.2	0.7	2.2	2.3	1.3	1.6	<0.5
Zr	290.5	192.8	160.8	214.7	60.3	2.4	281.5	209.9	309.1	223.5	0.3
Y	13.4	8.6	13.4	11.8	4.3	3.7	12.9	25.3	3.2	15.1	<0.1
La	58.3	81.7	23.5	54.5	83.4	145.7	31.5	32.6	49.7	31.1	3.4
Ce	81.6	127.4	45.3	84.8	111.0	170.4	55.6	56	75.9	53	5.3
Pr	7.29	13.27	4.26	8.27	7.35	11.69	5.22	6.4	6.89	5.71	0.45
Nd	22.5	39.5	12.6	74.6	15.8	26.9	15.7	23.4	22.8	20.1	1.6
Sm	3.26	3.67	2.38	3.1	1.42	2.08	2.22	4.47	3.64	2.96	0.24
Eu	0.44	0.46	0.52	0.47	0.30	0.35	0.41	1.07	0.61	0.57	0.04
Gd	2.28	1.63	2.13	2.01	1.45	1.45	1.8	4.75	1.26	2.22	0.08
Tb	0.37	0.26	0.35	0.33	0.24	0.22	0.33	0.72	0.13	0.39	<0.01
Dy	2.25	1.71	1.98	1.98	1.13	1.01	1.83	4.03	0.56	2.45	0.05
Ho	0.52	0.32	0.46	0.43	0.19	0.20	0.47	0.91	0.1	0.58	<0.02
Er	1.47	0.94	1.48	1.3	0.51	0.45	1.5	2.9	0.34	1.77	<0.03
Tm	0.23	0.14	0.24	0.2	0.06	0.04	0.23	0.4	0.08	0.27	<0.01
Yb	1.72	1.07	1.54	1.44	0.41	0.27	1.77	2.42	0.62	1.97	<0.05
Lu	0.3	0.21	0.29	0.27	0.07	0.05	0.31	0.48	0.11	0.34	<0.01
Mo	1.2	0.6	0.7	0.8	<0.1	<0.1	0.1	<0.1	<0.1	0.4	<0.1
Cu	2.7	1.1	5.3	3.0	1.6	0.4	5.3	8.6	<0.1	1.1	<0.1
Pb	99.9	0.7	7.6	36.1	12.0	11.3	3.1	8.4	2.7	10	0.2
Zn	3	<1	15	6.33	1	<1	7	28	<0.1	5	2
Ni	21.5	11.8	17.3	16.9	0.5	0.5	1.4	11.9	0.2	2.9	0.3
As	45	6.9	20.4	24.1	3.5	3.5	7.9	3.2	2.4	12.2	<0.5
Cd	<0.1	<0.1	0.1	0.1	<0.1	<0.1	<0.1	<0.1	<0.1	<0.1	<0.1
Sb	<0.1	<0.1	<0.1	0.1	<0.1	<0.1	<0.1	<0.1	<0.1	0.2	<0.1
Bi	<0.1	<0.1	<0.1	0.1	<0.1	<0.1	0.2	0.3	<0.1	<0.1	<0.1
Ag	<0.1	<0.1	<0.1	0.1	<0.1	<0.1	<0.1	<0.1	<0.1	<0.1	<0.1
Au (ppb)	1.9	1.6	4.5	2.7	2.3	1.6	2.4	2.1	1.9	1.2	2
Hg	0.11	0.06	0.03	0.07	1.09	0.36	7.54	0.03	1.31	1.32	9.55
Ti	<0.1	<1	0.2	0.13	<0.1	<0.1	<0.1	0.2	<0.1	<0.1	<0.1
Se	<0.5	<0.5	<0.5	0.5	<0.5	<0.5	<0.5	<0.5	<0.5	<0.5	<0.5

https://doi.org/10.1346/CCMN.2014.0620603 Published online by Cambridge University Press

Table 3 *contd*.

Major oxides (wt.%)	Altered tuff										
	OC2-1	OC2-7	OC2-8	OC2-9	OC2-12	OC2-13	OC2-15	OC3-2	OC3-4	OC3-8	Average
SiO_2	60.4	49.6	17.7	25.4	37	94.1	96.8	23.2	48.4	26	39.3
Al_2O_3	21.9	20.73	29.99	24.79	11.44	0.58	0.1	28.96	19.37	0.25	23.87
ΣFe_2O_3	1.12	4.14	0.15	6.06	28.77	0.13	0.2	1.62	8.08	1.21	4.71
MgO	0.23	0.3	0.26	0.25	0.25	0.18	0.11	0.54	2.5	30.48	0.66
CaO	0.15	0.24	0.02	0.03	0.02	0.01	0.02	0.07	2.05	8.08	0.55
Na_2O	0.56	0.73	2.21	1.19	0.23	0.02	0.07	1.86	0.52	<0.01	1.04
K_2O	0.82	2.13	5.36	5.24	2.73	0.06	<0.01	4.44	0.36	<0.01	2.69
MnO	<0.01	0.01	<0.01	<0.01	<0.01	<0.01	<0.01	<0.01	0.09	0.14	0.03
TiO_2	0.46	0.33	0.61	0.53	0.61	0.74	0.34	0.16	0.82	0.02	0.47
P_2O_5	0.1	0.13	0.87	0.82	0.89	0.03	<0.01	0.15	0.05	<0.01	0.33
Cr_2O_3	0.001	0.003	0.01	0.014	0.013	0.004	0.057	0.004	0.007	0.018	0.006
LOI	15.09	21.36	37.86	33.99	17.33	4.27	2.99	35.87	18.49	31.98	25.07
Total	100.86	99.78	95.39	98.52	99.61	100.14	100.78	97.03	100.75	98.18	98.8
TOT/C	0.03	0.02	0.1	0.09	0.06	0.02	0.03	0.16	0.06	8.85	0.06
TOT/S	1.79	3.99	11.99	9.91	4.66	0.09	0.05	10.23	0.06	0.03	5.43
SO_3	0.057	0.507	3.811	1.251	0.205	0.072	0.064	1.197	0.097	1.771	1.166
V_2O_5	0.005	0.02	0.034	0.049	0.068	0.004	0.004	0.023	0.031	0.004	0.028
Trace elements (ppm)											
Cu	<0.001	<0.001	<0.001	<0.001	<0.001	<0.001	<0.001	<0.001	0.002	<0.001	0.001
Ni	<0.001	<0.001	<0.001	<0.001	<0.001	<0.001	0.017	<0.001	0.004	0.004	0.005
Pb	<0.001	<0.001	0.007	0.004	0.013	<0.001	<0.001	<0.001	<0.001	<0.001	0.003
Sr	0.018	0.049	0.394	0.381	0.321	0.013	<0.002	0.09	0.011	0.002	0.135
Zn	0.001	0.003	0.002	0.002	0.003	0.003	0.003	0.002	0.008	0.002	0.004
Ba	511	614	3402	1887	3128	536	1705	961	349	64	1135
Be	<1	<1	1	1	1	<1	<1	<1	<1	1	1
Co	<0.2	0.7	0.2	<0.2	<0.2	<0.2	1.4	<0.2	19.9	2.9	2.84
Cs	39.3	25.8	20.3	16.8	36.3	17.2	1.2	13.4	3.3	<0.1	22.4
Ga	15.1	15.3	135.7	120.6	128.1	1.9	<0.5	17	19.1	<0.5	45.7
Hf	6.2	3.7	9.7	5.8	7.5	10.9	8.2	2.1	3.2	<0.1	5.5
Nb	12.7	9.1	17.8	12.4	17	25.1	8.8	4.5	5.7	<0.1	11.8
Rb	46.1	49.5	155	59.8	23.7	2.1	0.3	97.4	19.1	0.4	58.7
Sn	1	1	3	2	2	1	2	<1	1	<1	2
Sr	241.8	534.5	4044.8	4012.6	3292.9	71.9	12.6	942.9	109.2	37.9	1408.5
Ta	1.1	0.7	0.7	0.9	1.1	1.9	0.7	0.3	0.4	<0.1	0.8
Th	11.3	12.1	232.8	121.8	54.5	5.7	1.7	11.9	6	0.2	44.8
U	1.2	1.1	2.9	2.8	3	1.8	1	0.9	1	0.3	2.0
V	33	113	213	316	413	28	11	126	183	21	168
W	1.6	1.1	31.3	27.7	44	35.8	3.2	1	1.7	0.9	9.1
Zr	256.9	158	509.1	249.6	242.2	440.7	286.1	83.6	108.5	0.8	207.3
Y	2.7	2.5	5.6	5.8	8.6	7.1	1.7	2.2	18.6	3.1	8.5
La	20.6	36.5	456.7	385.6	376.8	22.8	1	30.5	14.4	1.9	130.4
Ce	36.5	68.5	439.2	321.5	451.7	19.8	1.3	47.1	44.2	3.9	148.5
Pr	4.52	5.87	35.92	25.52	36.86	2.16	0.11	3.54	3.61	0.53	12.24
Nd	11.8	11.5	88.2	76.2	91.2	6	<0.3	9	13.2	2.7	32.8
Sm	0.69	0.52	9.65	8	8.82	0.57	<0.05	0.72	3.01	0.5	3.71
Eu	0.08	0.05	1.89	1.3	1.62	0.12	<0.02	0.07	0.8	0.11	0.70
Gd	0.44	0.32	5.49	3.99	5.25	0.59	0.13	0.37	3.19	0.5	2.46
Tb	0.06	0.05	0.51	0.36	0.49	0.12	0.02	0.06	0.57	0.07	0.32
Dy	0.27	0.35	1.73	1.14	1.99	1.04	0.17	0.37	3.4	0.41	1.56
Ho	0.1	0.08	0.25	0.2	0.3	0.23	0.05	0.06	0.76	0.07	0.32
Er	0.28	0.27	0.58	1.49	0.93	0.97	0.21	0.26	2.26	0.22	1.04
Tm	0.06	0.04	0.11	0.13	0.13	0.15	0.02	0.04	0.36	0.03	0.15
Yb	0.54	0.44	0.99	0.95	1.07	1.22	0.25	0.31	2.54	0.17	1.10
Lu	0.09	0.06	0.17	0.16	0.16	0.23	0.06	0.06	0.38	0.02	0.19
Mo	0.3	0.5	0.2	8.2	6.5	0.2	4.8	0.3	<0.1	2.9	1.30
Cu	0.7	1.1	2.7	3.7	2	0.2	5.4	1.4	25.5	3.8	4.17
Pb	1.8	2.5	11.4	4.6	11.2	4.3	3.5	2.3	5.9	0.2	6.7
Zn	<1	2	1	2	<1	<1	<1	1	33	9	6.46
Ni	<0.1	0.3	4.1	6	2	1.6	151	1.3	9.6	66.2	3.14
As	1	26.7	34.6	229.7	459.5	6.8	<0.5	18.1	3.7	5.8	62
Cd	<0.1	<0.1	<0.1	<0.1	<1	<0.1	<0.1	<0.1	<0.1	<0.1	0.1
Sb	<0.1	<0.1	0.6	18	19.3	1.5	0.1	<0.1	0.1	0.6	2.9
Bi	<0.1	<0.1	<0.1	<0.1	1.2	0.4	<0.1	<0.1	0.1	<0.1	0.2
Ag	<0.1	<0.1	<0.1	<0.1	<0.1	<0.1	<0.1	<0.1	<0.1	<0.1	0.1
Au (ppb)	1	1.1	1.2	2.3	1.2	1	<0.5	1.2	3.6	2	1.8
Hg	0.05	0.04	4.85	2.61	2.97	0.22	10.98	1.08	0.08	0.4	1.79
Ti	<0.1	<0.1	0.3	0.3	1.2	0.3	<0.1	<0.1	<0.1	0.9	0.1
Se	<0.5	<0.5	<0.5	<0.5	0.8	<0.5	<0.5	<0.5	<0.5	<0.5	0.5

https://doi.org/10.1346/CCMN.2014.0620603 Published online by Cambridge University Press

Table 4. Mass gain and loss for the samples based on the composition (ppm) of average fresh composition and constant Zr.

Major oxides (wt.%)	Fresh tuff	Altered tuff	RC	ΔC_i
SiO_2	55.1	42.8	45.64	−9.46
Al_2O_3	11.14	18.3	25.46	14.32
ΣFe_2O_3	2.7	3.7	3.95	1.25
MgO	7.86	4.25	4.53	−3.33
CaO	0.48	0.9	0.96	0.48
Na_2O	0.9	0.8	0.85	−0.05
K_2O	2.94	2.1	2.24	−0.5
MnO	0.16	0.03	0.03	−0.13
TiO_2	0.42	0.43	0.46	0.04
P_2O_5	0.25	0.25	0.27	0.02
Cr_2O_3	0.011	0.009	0.009	−0.002
LOI	17.4	27.72	29.56	12.16
Total	99.58	96.32	102.72	3.14
TOT/C	1.59	0.57	0.61	−0.98
TOT/S	2.26	5.22	5.57	3.31
SO_3	0.776	3.51	3.74	2.96
V_2O_5	0.013	0.02	0.02	0.007
Trace elements (ppm)				
Cu	0.001	0.001	0.001	0
Ni	0.002	0.002	0.002	0
Pb	0.004	0.003	0.003	−0.001
Sr	0.066	0.11	0.11	0.044
Zn	0.004	0.003	0.003	−0.001
Ba	1804	1003.6	1070.3	−733.7
Be	1	1.12	1.19	0.19
Co	6.1	2.45	2.61	−3.49
Cs	23.1	18.24	19.41	−3.69
Ga	33.5	35.2	37.54	4.04
Hf	5.3	5.02	5.35	0.05
Nb	11.9	11.04	5.71	−6.19
Rb	81.2	45.03	48.02	−33.18
Sn	1	1.47	1.57	0.57
Sr	694.2	1097.7	1170.7	476.5
Ta	0.8	0.8	0.83	0.03
Th	34.4	34.75	37.1	2.7
U	3.3	1.75	1.87	−1.43
V	74	132.59	141.4	67.4
W	1.8	9.3	9.92	8.12
Zr	214.7	201.32	214.7	0
Y	11.8	7.21	7.69	−4.11
La	54.5	101.42	108.16	53.66
Ce	84.8	115.35	123.01	38.21
Pr	8.27	9.95	10.61	2.34
Nd	74.6	25.7	27.4	−47.2
Sm	3.1	2.92	3.11	0.01
Eu	0.47	0.55	0.59	0.12
Gd	2.01	1.96	2.12	0.11
Tb	0.33	0.26	0.28	−0.05
Dy	1.98	1.29	1.38	−0.6
Ho	0.43	0.27	0.29	−0.14
Er	1.3	0.9	0.96	−0.34
Tm	0.2	0.13	0.14	−0.06
Yb	1.44	0.94	1	−0.44
Lu	0.27	0.16	0.17	−0.1
Mo	0.8	1.47	1.57	0.77
Cu	3.0	3.75	3.4	0.4
Pb	36.1	5.61	5.98	−30.12
Zn	6.33	5.65	6.03	−0.3
Ni	16.9	15.29	16.31	−0.59
As	24.1	48.21	51.41	27.31
Cd	0.1	0.15	0.16	0.06
Sb	0.1	2.43	2.59	2.49
Bi	0.1	0.2	0.2	0.1
Ag	0.1	0.1	0.1	0
Au (ppb)	2.7	1.68	1.79	−0.91
Hg	0.07	2.62	2.79	2.72
Ti	0.13	0.26	0.28	0.15
Se	0.5	0.52	0.55	0.05

https://doi.org/10.1346/CCMN.2014.0620603 Published online by Cambridge University Press

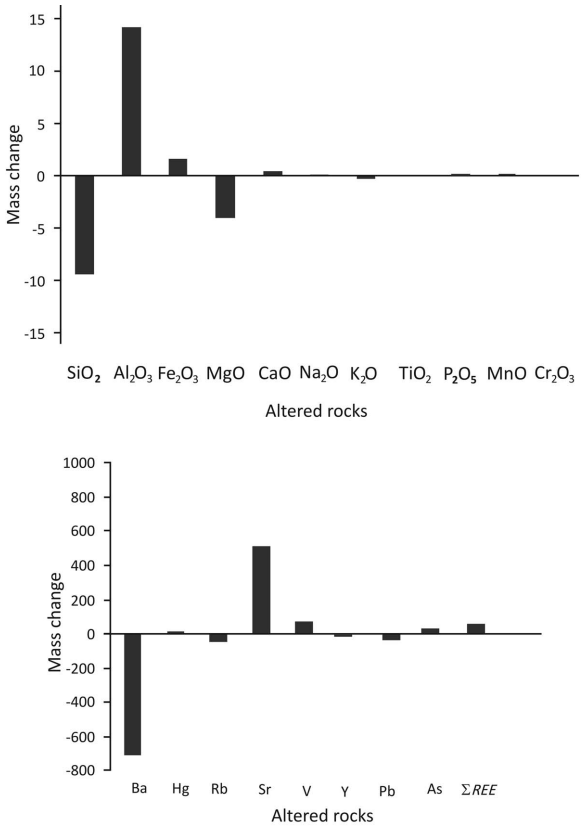

Figure 10. Mass change of the major elements (g/100 g) and trace elements (ppm/100 g) within the study area.

range from −150.09‰ to −123.61‰, and from −4.33‰ to −0.66‰, respectively. These isotopic data fall close to the left side of the kaolinite line in equilibrium with the meteoric waters at temperatures of >100ºC.

The sulfur- and oxygen-isotopic compositions of alunite range from 6.0‰ to 9.4‰ and from 5.5‰ to 10.3‰, respectively. These compositions reflect the involvement of steam-derived sulfur (Table 6; Figure 13; Hedenquist and Lowenstern, 1994; Rye, 2005).

DISCUSSION

The Güzelyurt kaolinite deposit of Aksaray is hosted by the Late Miocene Gördeles ignimbrite and consists of dacitic and andesitic tuffs. The kaolinite formed as a result of hydrothermal activity that developed along an active tectonic fault trending in a NE−SW direction. Lateral and vertical mineralogical zonation is characterized by a gradual transition from an inner kaolinite + alunite ± 7 Å halloysite zone outward to a smectite zone with increase of native sulfur and cinnabar-bearing alunite + 7 Å halloysite, and a porous silica zone upward through the sequences of kaolinite deposits. Fe-(oxyhydr)oxide phases associated with native sulfur and cinnabar demonstrate that multiple hydrothermal-alteration processes resulted in kaolinization and alunitization of the deposit. This inference is also supported by concentrations of Fe_2O_3 (max. 28.77%), SO_3 (max. 42.66%), Hg (max. 10.98 ppm), Ba (max. 3402 ppm), and Sr (max. 4045 ppm) in the altered volcanic units, which are similar to those reported by Nagasawa (1978) and Inoue (1995). The degradation of Fe-bearing hornblende and biotite results in iron oxidation which was found through petrographic determinations.

On the basis of textural and chemical analyses, argillization of feldspar and Fe-(oxyhydr)oxidation of hornblende and mica in the poorly welded, permeable, altered volcanic units are caused by an open hydrologic system. Thus, advanced alteration of feldspar, hornblende, biotite, and volcanic glass in the andesitic rocks resulted in an increase in the (Al ± Fe)/Si ratio and the leaching of alkali elements, which favors the precipitation of kaolinite or 7 Å halloysite under acidic

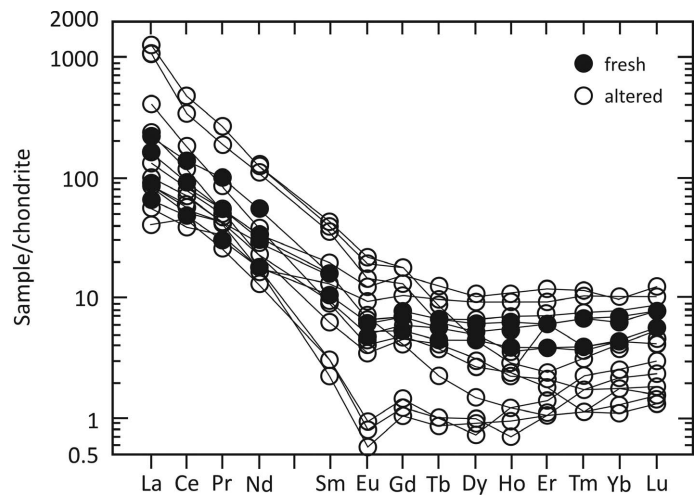

Figure 11. Chondrite-normalized *REE* patterns (Boynton, 1984) for fresh and altered samples from the study area.

https://doi.org/10.1346/CCMN.2014.0620603 Published online by Cambridge University Press

Table 5. Oxygen and hydrogen isotopic compositions of kaolinite, 7 Å halloysite, smectite, and kaolinite+smectite from the Güzelyurt kaolinite deposit.

Sample ID	Mineralogy	Weight (mg)	%H	Normalized δ^2H *vs.* VSMOW	%O	Normalized $\delta^{18}O$ *vs.* VSMOW
OC1-15	7 Å halloysite	0.755	0.42	–115.55	5.06	2.32
OC2-1	kaolinite	0.810	1.18	–106.05	13.09	0.84
OC2-2	7 Å halloysite	0.777	2.53	–101.81	42.20	7.64
OC1-2	kaolinite	0.789	1.22	–132.92	10.41	0.56
OC1-3	smectite	0.848	1.02	–136.91	8.30	–0.86
OC1-4	smectite	0.796	0.94	–123.61	7.97	–1.87
OC1-8	kaolinite+smectite	0.820	1.08	–130.49	9.55	–0.66
OC2-5	smectite	0.809	1.42	–150.09	11.83	–4.33

environmental conditions (Figure 14; Nagasawa, 1978; Meunier, 1995; Inoue, 1995; Kadir and Karakaş, 2002; Kadir *et al*., 2008).

The relative increase of the K/(Ca + Na) ratio and S (along with Al) resulted in the precipitation of authigenic alunite, with/without 7 Å halloysite, under acidic environmental conditions, similar to case studies in western Anatolia (Mutlu *et al*., 2005; Sayın, 2007; Ece and Schroeder, 2007; Ece *et al*., 2008). The relative increase in the S-H-bearing steam upward of the volcanic units resulted in an increase in the amount of alunite and 7 Å halloysite, rather than of kaolinite. This increase in the middle and upper parts of the deposit is controlled by hydrothermal processes at or above the water table by the oxidation of H_2S, with a relative increase in porosity and permeability upward of the volcanic units.

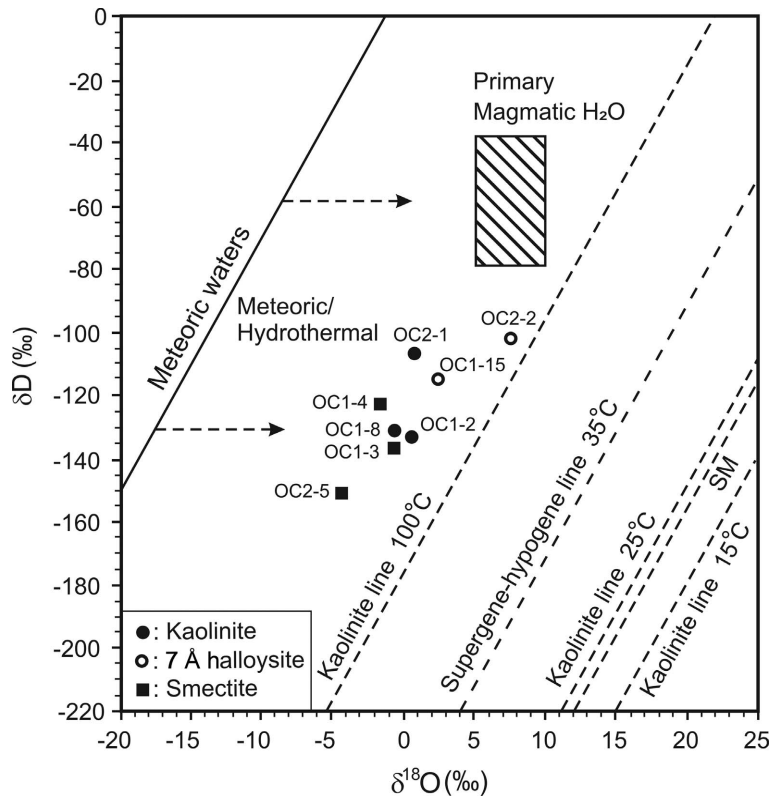

Figure 12. δD *vs*. $\delta^{18}O$ plot showing isotopic compositions of kaolinite, 7 Å halloysite, smectite, and kaolinite + smectite from the Güzelyurt kaolinite deposit (Sheppard, 1986). The kaolinite line in equilibrium with meteoric water at temperatures of 100ºC is from Hayba *et al*. (1985); those at 25ºC and 15ºC are from Sheppard and Gilg (1996). The supergene/hypogene line of kaolinite equilibrium with meteoric water at 35ºC is from Sheppard *et al.* (1969). The smectite line (SM) representing the isotopic composition in equilibrium with meteoric water at 20ºC is from Savin and Epstein (1970). The meteoric water line is from Craig (1961).

https://doi.org/10.1346/CCMN.2014.0620603 Published online by Cambridge University Press

Table 6. Oxygen and sulfur isotopic compositions of alunite samples from the Güzelyurt kaolinite deposit.

Sample	Mineralogy	$\delta^{34}S$ (‰)	$\delta^{18}O$ (‰)
OC1-1A	alunite	7.5	5.5
OC1-7	alunite	9.4	6.0
OC2-8	alunite	6.4	9.9
OC2-9	alunite	7.5	9.1
OC2-10	alunite	7.5	10.3
OC2-11	alunite	6.5	8.6
OC2-12	alunite	6.0	7.0

The concentration of released and depleted Mg, Si, Na, and Ca outward in the kaolinite deposit favored precipitation of smectite under alkaline micro-environmental conditions (Berner and Berner, 1996). Local concentrations of S- and Hg-bearing hydrothermal solutions caused the precipitation of native sulfur and cinnabar crystals in a reducing environment associated mainly with alunite or alunite/7 Å halloysite (Ece *et al*., 2013). The depletion of excess silica during alteration under low pressure and temperature and at neutral conditions occurred during hydrothermal fluid and steam flushing, and exhalations that happened close to the surface resulted in the development of a porous silica cap consisting of quartz and opal-CT (Ehrenberg, 1991; Rye *et al*., 1992; Herdianita *et al*., 2000; Meunier and Velde, 2004; Ece *et al*., 2013).

Micromorphologically, the occurrence of kaolinite as stacks in book-like form, the coexistence of 7 Å halloysite rods with alunite, and the development of subparallel orientation along fracture surfaces may reveal *in situ* dissolution and precipitation caused by hydrothermal-fluid flushing. The coexistence of trace gypsum with opal-CT in sample OC2-15 may be due to local increases in Ca and S that were brought about by siliceous hydrothermal-fluid injections. The sharp basal peaks and the reflections of non-basal doublets and triplets, euhedral hexagonal kaolinite, rod-like 7 Å halloysite identified by SEM and TEM, ideal DTA-TG curves, SiO_2/Al_2O_3 and SiO_2/R_2O_3 ratios (1.21 and 1.16; and 1.22 and 1.15), and chemical index of alteration (CIA) values between 94.23 and 97.30 in purified kaolinite and 7 Å halloysite samples suggest well crystallized kaolinite and 7 Å halloysite (Nesbitt and Markovics, 1997; Kadir and Karakaş, 2002; Sousa *et al.*, 2007).

Several different phases of hydrothermal activity in the study area caused changes in the reddish-brown coloration within the smectite-dominated altered volca-

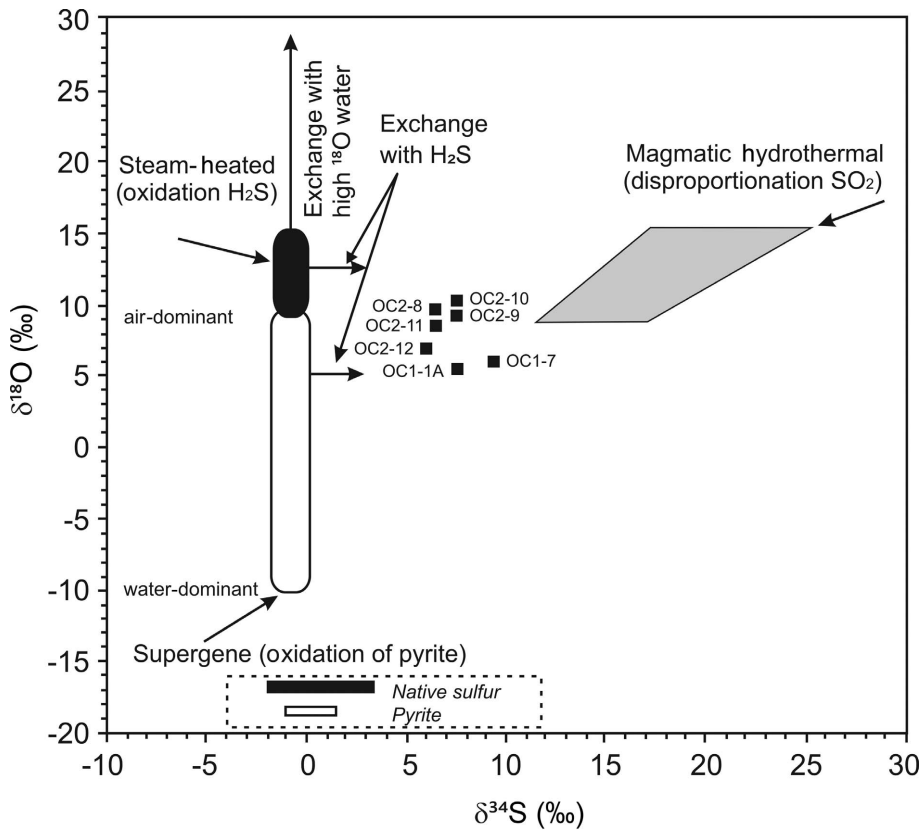

Figure 13. $\delta^{34}S$ *vs.* $\delta^{18}O$ plot showing isotopic compositions of alunite samples from the Güzelyurt kaolinite deposit (modified from Hedenquist and Lowenstern, 1994; Rye, 2005).

https://doi.org/10.1346/CCMN.2014.0620603 Published online by Cambridge University Press

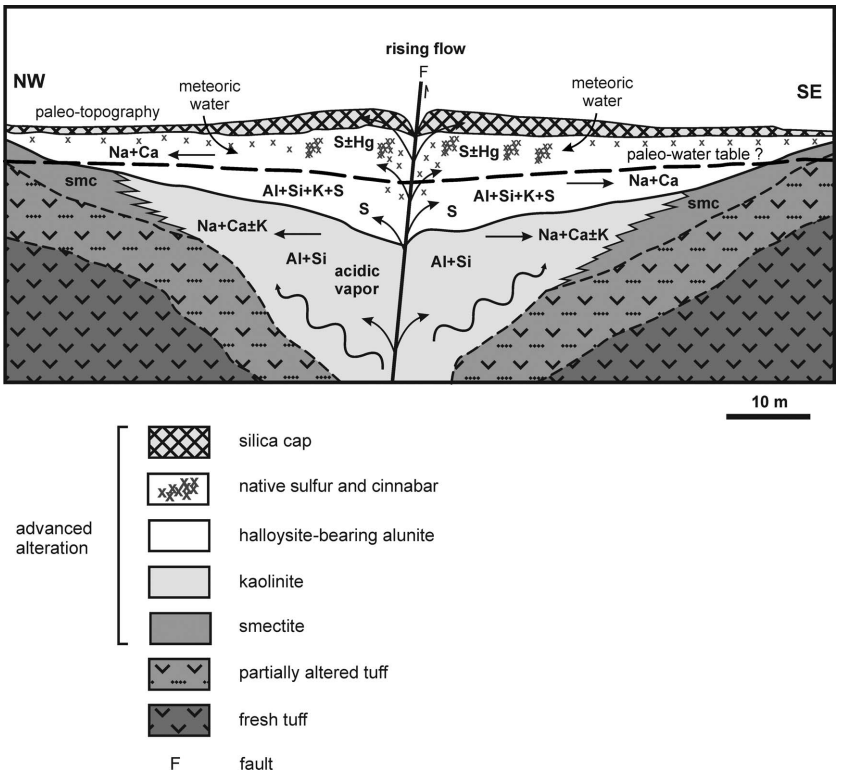

Figure 14. Genetic model for the Güzelyurt kaolinite deposit.

nites. The reddish-brown coloration was caused by Fe-(oxyhydr)oxide (Velde, 1985; Meunier, 2005).

The depletion of Si + Mg + K and Ba + Rb, the enhancement of Sr, the enrichment of *LREE*s relative to the *HREE*s, and the negative Eu anomalies reveal that the fractionation during alteration of plagioclase and hornblende and the devitrification of volcanic glass originated from dacitic and andesitic tuffs and basaltic lava during hydrothermal alteration processes and were the main sources of the kaolinite, 7 Å halloysite, and alunite formation (Rollinson, 1993).

The plot of δD and $\delta^{18}O$ values for the kaolinite + 7 Å halloysite fraction was between the equilibrium lines of kaolinite with meteoric water at 100ºC and with meteoric and primary magmatic water, but was near the equilibrium line of kaolinite with meteoric water at 100ºC; this may indicate a steam-heated environment at temperatures above 100ºC (Hayba *et al*., 1985; Ece *et al*., 2008, 2013). The isotopic data for kaolinite and 7 Å halloysite samples shifted to higher δD and $\delta^{18}O$ values, which were near the magmatic box compared with the smectitic samples; they may have been controlled by hydrothermal temperature changes and the degree of fractionation between the liquid and the vapor during the kaolinization and alunitization processes (Faure, 1986). A slight enrichment in the δD and $\delta^{18}O$ values of 7 Å halloysite from −115.55‰ to −101.81‰ and from 2.32‰ to 7.64‰, respectively, relative to kaolinite, which ranges from −132.92‰ to −106.05‰ and from 0.56‰ to 0.84‰, respectively, suggests the formation of kaolinite from steam-heated magmatic fluid and the formation of 7 Å halloysite ± kaolinite from the mixing of steam and meteoric water due to the exchange between the two fluids or evaporation (Gilg *et al*., 2003; Bethke *et al*., 2005; Deyell *et al*., 2005; Ece *et al*., 2013). Thus, the influence of meteoric water or the evaporation rate increase upward through the vertical sequences of the kaolinite deposit. This interpretation is also supported by the association of fine-grained alunite with 7 Å halloysite and the development of a porous silica cap at the uppermost layer of the kaolinite deposit (Deyell and Dipple, 2005; Rye, 2005). Lee *et al.* (2014) also noted that the high-sulfidation hydrothermal system of Seongsan (South Korea) exhibits similar enrichment, which is caused by the mixing of meteoric water with hydrothermal water.

Moreover, the positive $\delta^{34}S$ and $\delta^{18}O$ compositions of alunite, $\delta^{34}S$ values ranging between +6.0‰ and +9.4‰, and the fine grain sizes of alunite (<7 μm) reflect the involvement of steam-derived sulfur under temperatures of ~70−180ºC and pressures of 1−12 atm unlike that of magmatic steam which shows smaller $\delta^{34}S$ values (between +3.9 and +2.7), coarser grain sizes (>50 μm) and higher temperatures (200−300ºC) (Rye *et al*., 1992; Rye, 2005; Deyell and Dipple, 2005; Lerouge *et al*., 2006; Georgieva and Velinova, 2012). This

https://doi.org/10.1346/CCMN.2014.0620603 Published online by Cambridge University Press

suggestion was also supported by the absence of pyrite, dickite, and pyrophyllite in association with alunite which might be expected at higher temperatures (200–340ºC) (Deyell and Dipple, 2005).

CONCLUSION

The Güzelyurt kaolinite deposit was formed by the hydrothermal alteration of dacitic and andesitic tuffs and basaltic lavas and was controlled by tectonic activity. These alteration processes resulted in a mineralogical zonation outward from the main kaolinite deposit. This outward zonation is: kaolinite + alunite ± 7 Å halloysite, smectite, the occurrence of a silica cap (opal-CT, quartz), and Fe-(oxyhydr)oxide phases associated with native sulfur and cinnabar above the deposit. This demonstrates that the kaolinization and alunitization were the result of multiple hydrothermal-alteration processes. The occurrence of kaolinite below, and alunite + 7 Å halloysite associated with native sulfur and cinnabar in the middle and above, the deposit suggests that alunite formed following the precipitation of kaolinite from a sulfur-rich hydrothermal fluid and under steam flushing and exhalative conditions. The increase in the (Al_2O_3 + Fe_2O_3 + K_2O)/SiO_2 ratio and the decrease in MgO + Na_2O + CaO along the fault zone also support the hydrothermal-zonation hypothesis. Micromorphologically, the development of platy and book-like kaolinite, the coexistence of rod-like 7 Å halloysite and cubic alunite with relicts of volcanogenic materials, the depletion of Si + Mg + K, Rb + Ba, the enrichment of S and Sr, the depletion of the *HREE* relative to the *LREE*, and a negative Eu anomaly suggest that these minerals formed from the alteration of feldspar, hornblende, and volcanic glass by a dissolution-precipitation mechanism under acidic environmental conditions in an open hydrologic system. A relative increase in the δD and $\delta^{18}O$ values of kaolinite and 7 Å halloysite above the deposit reflects the mixing of magmatic and meteoric waters and evaporation. The positive $\delta^{34}S$ and $\delta^{18}O$ isotope compositions of alunite with fine grain sizes suggest its formation under the influence of steam-derived sulfur from the oxidation of H_2S at or above the water table.

ACKNOWLEDGMENTS

This present study was supported financially by the Scientific Research Projects Fund of Eskişehir Osmangazi University in the framework of Project 201015030. The authors are indebted to Professor Warren D. Huff and an anonymous reviewer for their careful and constructive reviews that improved the quality of the paper significantly. The authors are also grateful to Associate Editor, Robert J. Pruett, Editors in Chief, Michael A. Velbel and Joseph W. Stucki, and Managing Editor, Kevin Murphy for their insightful editorial comments and suggestions. This paper was presented at the 50th Anniversary Annual Meeting of The Clay Minerals Society, University of Illinois at Urbana-Champaign, Illinois, USA.

REFERENCES

Arslan, M., Kadir, S., Abdioğlu, E., and Kolaylı, H. (2006) Origin and formation of kaolin minerals in saprolite of Tertiary alkaline volcanic rocks, Eastern Pontides, NE Turkey. *Clay Minerals*, **41**, 597–617.

Berner, E.K. and Berner, R.A. (1996) *Global Environment: Water, Air, and Geochemical Cycles*. Princeton University Press, New Jersey, USA, 376 pp.

Bethke, P.M., Rye, R.O., Stoffregen, R.E., and Vikre, P.G. (2005) Evolution of the magmatic-hydrothermal acid-sulfate system at Summitville, Colorado: integration of geological, stable-isotope, and fluid-inclusion evidence. *Chemical Geology*, **215**, 281–315.

Brindley, G.W. (1980) Quantitative X-ray analysis of clays. Pp. 411–438 in: *Crystal Structures of Clay Minerals and their X-ray Identification* (G.W. Brindley and G. Brown, editors). Monograph **5**, Mineralogical Society, London.

Boynton, W.V. (1984) Cosmochemistry of the rare earth elements: meteorite studies. Pp. 63–114 in: *Rare Earth Element Geochemistry* (P. Henderson, editor), Developments in Geochemistry. Elsevier, Amsterdam.

Chen, Y.C., Wang, M.K., and Yang, D.S. (2001) Mineralogy of dickite and nacrite from northern Taiwan. *Clays and Clay Minerals*, **49**, 586–595.

Clayton, R.N. and Mayeda, T.K. (1963) The use of bromine pentafluoride in the extraction of oxygen from oxides and silicates for isotopic analysis. *Geochimica et Cosmochimica Acta*, **27**, 43–52.

Craig, H. (1961) Isotopic variations in meteoric waters. *Science*, **133**, 1702–1703.

Deyell, C.L. and Dipple, G.M. (2005) Equilibrium mineral-fluid calculations and their application to the solid solution between alunite and natroalunite in the El Indio-Pascua belt of Chile and Argentina. *Chemical Geology*, **215**, 219–234.

Deyell, C.L., Rye, R.O., Landis, G.P., and Bissig, T. (2005) Alunite and the role of magmatic fluids in the Tambo high-sulfidation deposit, El Indio-Pascua belt, Chile. *Chemical Geology*, **215**, 185–218.

Dönmez, M., Akçay, A.E., Kara, H., Türkecan, A., and Yergök, F.A. (2005) *Geological map of Aksaray L32 Quadrangle, Scale 1:100.000.* General Directorate of Mineral Research and Exploration (MTA) Publications, Ankara.

Ece, Ö.İ. and Schroeder, P.A. (2007) Clay mineralogy and chemistry of halloysite and alunite deposits in the Turplu area, Balikesir, Turkey. *Clays and Clay Minerals*, **55**, 18–35.

Ece, Ö. İ., Schroeder, P.A., Smilley, M., and Wampler, M. (2008) Acid-sulfate alteration volcanic rocks and genesis of halloysite and alunite deposits in the Biga Peninsula, NW Turkey. *Clay Minerals*, **43**, 281–315.

Ece, Ö.İ., Ekinci, B., Schroeder, P.A., Crowe, D., and Esenli, F. (2013) Origin of the Düvertepe kaolin-alunite deposits in Simav Graben, Turkey: Timing and styles of hydrothermal mineralization. *Journal of Volcanology and Geothermal Research*, **255**, 57–18.

Ehrenberg, S.N. (1991) Kaolinized, potassium-leached zones at the contacts of the Garn Formation, Haltenbanken, mid-Norwegian continental shelf. *Marine and Petroleum Geology*, **8**, 250–269.

Erkoyun, H. and Kadir, S. (2011) Mineralogy, micromorphology, geochemistry and genesis of a hydrothermal kaolinite deposit and altered Miocene host volcanites in the Hallaçlar area, Uşak, western Turkey. *Clay Minerals*, **46**, 421–448.

Faure, G. (1986) *Principles of Isotope Geology*, 2nd edition, John Wiley and Sons, New York, 589 pp.

Fujii, N., Kayabalı, İ., and Saka, A.H. (1995) *Data Book of Ceramic Raw Materials of Selected Areas in Turkey*.

Monograph Series No.**1**, General Directorate of Mineral Research and Exploration, Ankara, 144 pp.

Georgieva, S. and Velinova, N. (2012) Alunite from the advanced argillic alterations in the Chelopech high-sulphidation epithermal Cu-Au deposit, Bulgaria: Chemistry, morphology and genetic significance. *Geochemistry, Mineralogy and Petrology*, **49**, 17–31.

Gilg, H.A., Weber, B., Kasbohm, J., and Frei, R. (2003) Isotope geochemistry and origin of illite-smectite and kaolinite from the Seiltz and Kemmlitz kaolin deposits, Saxony, Germany. *Clay Minerals*, **38**, 95–112.

Hayba, D.O., Bethke, P.M., Heald, P., and Faley, N.K. (1985) Geologic, mineralogic and geochemical characteristics of volcanic-hosted epithermal precious-metal deposits. *Reviews in Economic Geology*, **2**, 129–167.

Hedenquist, J.W. and Lowenstern, J.B. (1994) The role of magmas in the formation of hydrothermal ore deposits. *Nature*, **370**, 519–527.

Herdianita, N.R., Browne, P.R.L., Rodgers, K.A., and Campbell, K.A. (2000) Mineralogical and textural changes accompanying ageing of silica sinter. *Mineralium Deposita*, **35**, 48–62.

Hosono, T., Lorphensriand, O., Onodera, S-i, Okawa, H., Nakano, T., Yamanaka, T., Tsujimura, M., and Taniguchi, M. (2014) Different isotopic evolutionary trends of $\delta^{34}S$ and $\delta^{18}O$ compositions of dissolved sulfate in an anerobic deltaic aquifer system. *Applied Geochemistry*, **46**, 30–42.

Imai, N., Otsuka, R., and Kashide, H. (1969) Dehydration of palygorskite and sepiolite from the Kuzu District, Tochigi Pref., central Japan. Pp. 99–108 in: Proceedings, International Clay Conference, Tokyo.

Inoue, A. (1995) Formation of Clay Minerals in Hydrothermal Environments. Pp. 268–329 in: *Origin and Mineralogy of Clays* (B. Velde, editor), Springer-Verlag Berlin.

Jones, B.F. and Galán, E. (1988) Sepiolite and palygorskite. Pp. 631–674 in: *Hydrous Phyllosilicates (Exclusive of Micas)* (S.W. Bailey, editor). Reviews in Mineralogy, **19**, Mineralogical Society of America, Washington, D.C.

Jepson, W.B. and Rowse, J.B. (1975) The composition of kaolinite; an electron microscope microprobe study. *Clays and Clay Minerals*, **23**, 310–317.

Kadir, S. and Akbulut, A. (2009) Mineralogy, geochemistry and genesis of the Taşoluk kaolinite deposits in pre-Early Cambrian metamorphites and Neogene volcanites of Afyonkarahisar, Turkey. *Clay Minerals*, **44**, 89–112.

Kadir, S. and Erkoyun, E. (2013) Genesis of the hydrothermal Karaçayır kaolinite deposit in Miocene volcanics and Palaeozoic metamorphic rocks of the Uşak-Güre basin, Western Turkey. *Turkish Journal of Earth Sciences*, **22**, 444–468.

Kadir, S. and Karakaş, Z. (2002) Mineralogy, chemistry and origin of halloysite, kaolinite and smectite from Miocene ignimbrites, Konya, Turkey. *Neues Jahrbuch für Mineralogie, Abhandlungen*, **177**, 113–132.

Kadir, S., Önen-Hall, P., Aydin, S.N., Yakicier, C., Akarsu, N., and Tuncer, M. (2008) Environmental effect and genetic influence: a regional cancer predisposition survey in the Zonguldak region of northwest Turkey. *Environmental Geology*, **54**, 391–409.

Kadir, S., Erman, H., and Erkoyun, H. (2011) Mineralogical and geochemical characteristics and genesis of hydrothermal kaolinite deposits within Neogene volcanites, Kütahya (western Anatolia), Turkey. *Clays and Clay Minerals*, **59**, 250–276.

Küçüksille, N. (1979) Report on alunite-bearing kaolinite deposits at Güzelyurt, Niğde-Aksaray. MTA Report No. 6500, Ankara (in Turkish).

Lanson, B., Beaufort, D., Berger, G., Bauer, A., Cassagnabère, A., and Meunier, A. (2002) Authigenic kaolin and illitic minerals during burial diagenesis of sandstones: a review. *Clay Minerals*, **37**, 1–22.

Lee, G., Koh, S.M., and Pirajno, F.M. (2014) Evolution of hydrothermal fluids of HS and LS type epithermal Au-Ag deposits in the Seongsan hydrothermal system of the Cretaceous Haenam volcanic field, South Korea. *Ore Mineralogy Reviews*, **61**, 33–51.

Lerouge, C., Kunov, A., Fléhoc, C., Georgieva, S., Hikov, A., Lescuyer, J.K, Petrunov, R., and Velinova, N. (2006) Constraints of stable isotopes on the origin of alunite from advanced argillic alteration systems in Bulgaria. *Journal of Geochemical Exploration*, **90**, 166–182.

MacKenzie, R.C. (1957) *The Differential Thermal Investigation of Clays*. Monograph **2**, Mineralogical Society, London, 456 pp.

MacLean, W.H. and Kranidiotis, P. (1987) Immobile elements as monitors of mass transfer in hydrothermal alteration: Phelps Dodge massive sulfide deposits, Matagami, Quebec. *Economic Geology*, **2**, 951–962.

Meunier, A. (1995) Hydrothermal alteration by veins. Pp. 247–267 in: *Origin and Mineralogy of Clays, Clays and the Environment* (B. Velde, editor). Springer-Verlag, Berlin.

Meunier, A. (2005) *Clays*. Springer-Verlag, Berlin, Heidleberg, 472 pp.

Meunier, A. and Velde, B. (2004) *Illite: Origin, Evolution and Metamorphism*. Springer-Verlag, Berlin, Heidelberg, New York, 286 pp.

Moore, D.M. and Reynolds, R.C. (1989) *X-ray Diffraction and the Identification and Analysis of Clay Minerals*. Oxford University Press, New York, 332 pp.

Mutlu, H., Sarıiz, K., and Kadir, S. (2005) Geochemistry and origin of the Şaphane alunite deposit, Western Anatolia, Turkey. *Ore Geology Reviews*, **26**, 39–50.

Nagasawa, K. (1978) Kaolin minerals. Pp. 189–219 in: *Clays and Clay Minerals of Japan* (T. Sudo and S. Shimoda, editors). Developments in Sedimentology, **26**, Elsevier, Tokyo.

Nesbitt, H.W. and Markovics, G. (1997) Weathering of granidioritic crust, long-term storage of elements in weathering profiles and petrogenesis of siliciclastic sediments. *Geochimica et Cosmochimica Acta*, **61**, 1653–1670.

Njoya, A., Nkoumbou, C., Grosbois, C., Njopwouo, D., Njoya, D., Courtin-Nomade, A., Yvon, J., and Martin, F. (2006) Genesis of Mayouom kaolin deposit (western Cameroon). *Applied Clay Science*, **32**, 125–140.

Paterson, E. and Swaffield, R. (1987) Thermal analysis. Pp. 99–132 in: *A Handbook of Determinative Methods in Clay Mineralogy* (M.J. Wilson, editor). Blackie and Sons Limited, Glasgow, UK, 308 pp.

Rollinson, H.R. (1993) *Using Geochemical Data: Evaluation, Presentation, Interpretation*. John Wiley and Sons Inc., New York, 352 pp.

Rye, R.O. (2005) A review of the stable-isotope geochemistry of sulfate minerals in selected igneous environments and related hydrothermal systems. *Chemical Geology*, **215**, 5–36.

Rye, R.O., Bethke, P.M., and Wasserman, M.D. (1992) The stable isotope geochemistry of acid sulfate alteration. *Economic Geology*, **87**, 225–255.

Savin, S.M. and Epstein, S. (1970) The oxygen and hydrogen isotope geochemistry of clay minerals. *Geochimica et Cosmochimica Acta*, **34**, 25–42.

Sayın, Ş.A. (2007) Origin of kaolin deposits: evidence from the Hisarcık (Emet-Kütahya) deposits, western Turkey. *Turkish Journal of Earth Sciences*, **16**, 77–96.

Sheppard, S.M.F. (1986) Characterization and isotopic variations in natural waters. Pp. 141–162 in: *Stable Isotopes in High Temperature Geological Processes* (J.W. Valley, H.P. Taylor, and J.R. O'Neil, editors). Reviews in Mineralogy,

16, Mineralogical Society of America, Washington, D.C.
Sheppard, S.M.F. and Gilg, H.A. (1996) Stable isotope geochemisty of clay minerals. *Clay Minerals*, **31**, 1–24.
Sheppard, S.M.F., Nielsen, R.L., and Taylor, H.P. (1969) Oxygen and hydrogen isotope ratios of clay minerals from porphyry copper deposits. *Economic Geology*, **64**, 755–777.
Smykatz-Kloss, W. (1974) *Differential Thermal Analysis, Application and Results in Mineralogy*. Springer-Verlag, Berlin, 185 pp.
Sousa, D.J.L., Varajão, A.F.D.C., Yvon, J., and Da Costa, G.M. (2007) Mineralogical, micromorphological and geochemical evolution of the kaolin facies deposit from the Capim region (northern Brazil). *Clay Minerals*, **42**, 69–87.
Temel, A., Gençoğlu, H., Bayhan, H., Öner, F., and Ağrılı, H. (1995) Mekedere (Güzelyurt – Aksaray) kaolinit ocağının hidrotermal mineral oluşumları. *VII. Ulusal Kil Sempozyumu Bildiriler Kitabı*, s. 76–87.
Velde, B. (1985) *Clay Minerals. A Physico-Chemical Explanation of their Occurrence*. Development in Sedimentology, **40**, Elsevier, New York, 427 pp.
Wilson, M.J. (1987) X-ray powder diffraction methods. Pp. 26–98 in: *A Handbook of Determinative Methods in Clay Mineralogy* (M.J. Wilson, editor). Blackie & Sons, Glasgow and London.
Yuan, J. and Murray, H.H. (1993) Mineralogical and physical properties of the Maoming kaolin from Guangdong province, south China. Pp. 249–259 in: *Kaolin Genesis and Utilization* (H.H. Murray, W.M. Bundy, and C.C. Harvey, editors). The Clay Minerals Society, Boulder, Colorado, USA.

(*Received 19 February 2014; revised 26 December 2014; Ms. 851; AE: R.J. Pruett*)